

# Kinetic Inductance, Quantum Geometry, and Superconductivity in Magic-Angle Twisted Bilayer Graphene

Miuko Tanaka<sup>1,2,†</sup>, Joel Î-j. Wang<sup>1,†\*</sup>, Thao H. Dinh<sup>3</sup>, Daniel Rodan-Legrain<sup>1</sup>, Sameia Zaman<sup>1,4</sup>, Max Hays<sup>1</sup>, Bharath Kannan<sup>1,4,8</sup>, Aziza Almanakly<sup>1,4</sup>, David K. Kim<sup>5</sup>, Bethany M. Niedzielski<sup>5</sup>, Kyle Serniak<sup>1,5</sup>, Mollie E. Schwartz<sup>5</sup>, Kenji Watanabe<sup>6</sup>, Takashi Taniguchi<sup>7</sup>, Jeffrey A. Grover<sup>1</sup>, Terry P. Orlando<sup>1,4</sup>, Simon Gustavsson<sup>1,8</sup>, Pablo Jarillo-Herrero<sup>3\*</sup>, and William D. Oliver<sup>1,3,4\*</sup>

<sup>1</sup>*Research Laboratory of Electronics, Massachusetts Institute of Technology, Cambridge, MA 02139, USA*

<sup>2</sup>*Institute for Solid State Physics, The University of Tokyo, 5-1-5 Kashiwanoha, Kashiwa, Chiba, Japan*

<sup>3</sup>*Department of Physics, Massachusetts Institute of Technology, Cambridge, MA 02139, USA*

<sup>4</sup>*Department of Electrical Engineering and Computer Science, Massachusetts Institute of Technology, Cambridge, MA 02139, USA*

<sup>5</sup>*Lincoln Laboratory, Massachusetts Institute of Technology, 244 Wood Street, Lexington, MA 02421, USA*

<sup>6</sup>*Research Center for Electronic and Optical Materials, National Institute for Materials Science, 1-1 Namiki, Tsukuba 305-0044, Japan*

<sup>7</sup>*Research Center for Materials Nanoarchitectonics, National Institute for Materials Science, 1-1 Namiki, Tsukuba 305-0044, Japan*

<sup>8</sup>*Present address: Atlantic Quantum, Cambridge, MA 02139, USA*

<sup>†</sup>These authors contributed equally to this work.

\*To whom correspondence should be addressed: [joelwang@mit.edu](mailto:joelwang@mit.edu), [pjarillo@mit.edu](mailto:pjarillo@mit.edu), and [william.oliver@mit.edu](mailto:william.oliver@mit.edu)

# Abstract

The physics of superconductivity in magic-angle twisted bilayer graphene (MATBG) is a topic of keen interest in moiré systems research, and it may provide insight into the pairing mechanism of other strongly correlated materials such as high- $T_c$  superconductors. Here, we use DC-transport and microwave circuit quantum electrodynamics (cQED) to measure directly the superfluid stiffness of superconducting MATBG via its kinetic inductance. We find the superfluid stiffness to be much larger than expected from conventional single-band Fermi liquid theory; rather, it aligns well with theory involving quantum geometric effects that are dominant at the magic angle.<sup>1</sup> The temperature dependence of the superfluid stiffness exhibits a power-law behavior, which contraindicates an isotropic BCS model; instead, the extracted power-law exponents indicate an anisotropic superconducting gap, whether interpreted using the conventional anisotropic BCS model or a quantum geometric theory of flat-band superconductivity. Moreover, the quadratic dependence of the stiffness on both DC and microwave current is consistent with Ginzburg-Landau theory. Taken together, these findings strongly suggest a connection between quantum geometry, superfluid stiffness, and unconventional superconductivity in MATBG. Finally, the combined DC-microwave measurement platform used here is applicable to the investigation of other atomically thin superconductors.

# Main

## Introduction

Stacking two graphene sheets with a finite twist angle between individual crystallographic axes forms a moiré superlattice. As the twist angle is reduced, the constituent monolayers' electronic structures hybridize, forming flat bands near the so-called magic angle of 1.05 degrees (the first magic angle). These flat bands facilitate strong electron-electron interactions in graphene, which lead to a wealth of different phases of matter, including correlated insulators, superconductors, strange-metal phases, and topological insulating states, all accessible via an applied gate-voltage that controls the carrier density.<sup>2-5</sup>

Of particular interest is the superconductivity observed in magic-angle twisted bilayer graphene (MATBG) or magic-angle twisted multi-layer graphene (MATMG),<sup>6-10</sup> as their phase diagrams share a notable resemblance to unconventional superconductors, including cuprates and heavy-fermion superconductors.<sup>3,5,11,12</sup> The ratio reaching 0.1 between the critical temperature  $T_C$  and the Fermi temperature  $T_F$  is comparable to that of unconventional superconductors in the strong-coupling regime.<sup>3,5,6</sup> Furthermore, superconductivity is observed in the flat-band regions of MATBG, suggesting that it is driven by strong Coulomb interactions.

Given these apparent similarities, it is conceivable that gaining a deeper understanding into the mechanism underlying superconductivity in MATBG or MATMG could lead to fundamental insights into other unconventional superconductors and strongly correlated systems. These observations lead us to a fundamental question: how does superconductivity arise in a flat-band system, where due to the large effective mass, the conventional single-band Fermi-liquid and BCS theories start to breakdown?<sup>13–15</sup> Theoretical studies have proposed – and we shall provide supporting experimental evidence here – that the origin of superconductivity in a flat-band system is connected to its “quantum geometry” as characterized by the quantum geometric tensor.<sup>1,13–16</sup>

Addressing this question experimentally is challenging, as many unconventional superconductors are bulk crystals with properties that can only be tuned by altering the material composition over many samples. In contrast, magic-angle moiré superlattices can explore a wide swath of the phase-space essentially via the back-gate voltage on a single device. However, despite this apparent experimental simplicity, to date, there have been relatively few experimental investigations of the unconventional pairing in moiré superconducting systems. Many of the conventional techniques used to study the gap structure of bulk superconductors, such as magnetic penetration depth, Meissner effect, thermal transport, and inelastic neutron scattering, are difficult to apply to van der Waals (vdW) heterostructures made by mechanical exfoliation. This is due in part to the small size of typical 2D samples – atomically thin with a few-micron-square area and an inhomogeneous twist angle – and also their generally ultra-low carrier density.

Scanning-tunneling microscope (STM) studies have indicated an unconventional, nodal-like gap in the superconducting phase of magic-angle twisted bilayer- and trilayer-graphene based on a BCS theory involving Dyne’s formula in an extended s-wave framework.<sup>11,17</sup> In addition, a Josephson junction was recently used to probe the quasiparticle dynamics and thermalization rates in MATBG, favoring an anisotropic or nodal pair state in MATBG,<sup>18</sup> but also derived using a BCS framework. In a complementary work using DC quantum transport measurements, Tian *et al.*, found evidence that the superfluid stiffness in flat-band MATBG was consistent with a quantum geometric interpretation.<sup>19</sup>

Here, we use a microwave resonator terminated by MATBG to measure the kinetic inductance – and thereby the superfluid stiffness – of MATBG near and within the flat-band regime. The kinetic inductance can be interpreted as the “inertia” of charge carriers when a material is subject to a time-dependent electric field. The associated kinetic energy of the carriers is stored in the form of inductive energy of the element, resulting in the kinetic inductance  $L_K$  that contributes to the total inductance  $L = L_K + L_G$ , where  $L_G$  is the geometric inductance of the circuit element.

Kinetic inductance is the inverse of the superfluid stiffness  $D_s$ , which governs the electromagnetic properties in superconducting materials via the constitutive relation (in the London gauge)

$$\mathbf{j} = -D_s \mathbf{A}, \quad (1)$$

where  $\mathbf{j}$  is the 2D current density (current per unit width), and  $\mathbf{A}$  is the vector potential.<sup>20</sup> For a superconductor in the clean limit, where the superconducting coherence length is shorter than the scattering length, the sheet kinetic inductance  $L_{K/\square}$  can be expressed as follows based on single-band Fermi liquid theory:

$$L_{K/\square} = 1/D_s = \frac{m_{\text{eff}}}{2n_s e^2}, \quad (2)$$

where  $n_s$  is the 2D superfluid density and  $m_{\text{eff}}$  is the effective mass of the charge carrier in a superconductor.<sup>20</sup> The temperature dependence of  $n_s$  is characteristic of the pairing symmetry and gap structure in the superconductor due to its quasiparticle spectrum at finite temperature. Characterizing the kinetic inductance is hence a promising tool to study the nature of superconductivity as it grants direct access to the superfluid stiffness and thereby the superfluid density  $n_s$ , presuming a particular model that connects them.

In this work, we measure directly the superfluid stiffness via the kinetic inductance  $L_K$  and its dependence on temperature, DC bias current, and microwave power. The measured superfluid stiffness is much larger than expected from conventional single-band Fermi liquid theory, instead aligning well with theory incorporating quantum geometric effects that are expected to dominate at the magic angle.<sup>1</sup> Furthermore, the temperature dependence of the superfluid stiffness exhibits a power-law behavior that contraindicates a BCS isotropic model and supports the quantum-metric origin of flat-band superconductivity. And, the quadratic dependence of the stiffness on both DC and microwave current is consistent with Ginzburg-Landau theory. Taken together, our results indicate a quantum-geometric origin of unconventional superconductivity in the strongly interacting, flat-band region of MATBG.

## Device Configuration

We use a superconducting quarter-wavelength ( $\lambda/4$ ) waveguide resonator to characterize the kinetic inductance of MATBG (Fig. 1). When a resonator is terminated directly to ground, it has a resonance frequency  $f = \frac{1}{2\pi\sqrt{L_{\text{eff}}C_{\text{eff}}}}$ , where  $L_{\text{eff}}$  and  $C_{\text{eff}}$  are the effective inductance and capacitance of the resonator, respectively. When a resonator is terminated to ground through a MATBG sample, the resonance frequency shifts to a new frequency  $f' = \frac{1}{2\pi\sqrt{(\tilde{L}_{\text{eff}}(V_{\text{BG}}))C_{\text{eff}}}}$  due to the appreciable kinetic inductance of the MATBG added

to the resonator’s intrinsic inductance, where  $\tilde{L}_{\text{eff}}$  is the gate-dependent effective inductance of the hybrid resonator. As we describe below, the added inductance of the MATBG sample can be extracted from shifts in the resonance frequency (Fig. 1a).

Fig. 1b shows the superconducting resonators used in this experiment. The resonators are patterned from a 250-nm aluminum film deposited on a high-resistivity silicon substrate. A common throughline couples capacitively to both a “control” and an “experiment” resonator and is used to measure their resonance frequencies. The control resonator is solely used to assess if the MATBG fabrication has impacted the aluminum fabrication process. The MATBG sample that terminates the experiment resonator is an hBN-MATBG-hBN heterostructure (Fig. 1c) positioned on an aluminum backgate, to which a voltage is applied to tune the MATBG carrier density. In addition, five galvanic contacts are made to the microwave resonator, the ground plane, and three DC probe electrodes (Fig. 1c) using a 1D edge-contact technique comprising titanium/aluminum.<sup>21</sup> This design enables us to perform both microwave and DC transport characterization of the MATBG device.

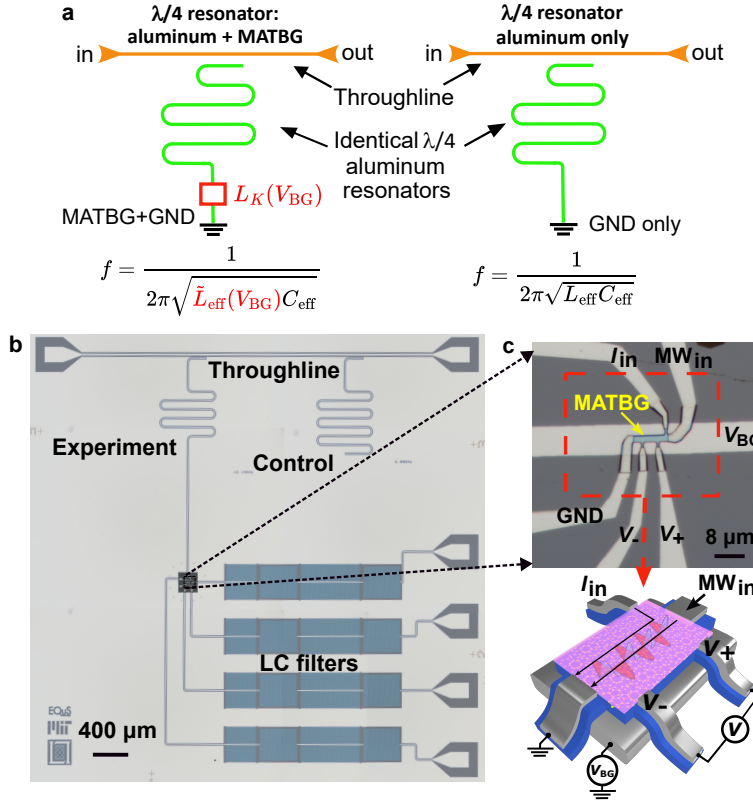


Figure 1: **Kinetic inductance measurement and device configuration.** **a**, Schematic of the magic angle twisted bilayer graphene (MATBG) inductance measurement circuit. The experiment resonator terminates to ground through the MATBG sample. The control resonator terminates directly to ground and is used solely to check for adverse effects arising from the MATBG fabrication process. Both resonators couple capacitively to the throughline, which is probed by a network analyzer (not shown) to measure the resonance frequencies. The resonance frequency of the experiment resonator is used to infer the gate-voltage-dependent inductance of the MATBG. **b**, Optical image of a  $5 \times 5 \text{ mm}^2$  chip comprising the resonators, throughline, DC bias lines, filters, and the ground plane, patterned from 250-nm thick aluminum on a high-resistivity Si substrate. The DC electrodes are LC-filtered on-chip to reduce bias noise. **c**, Zoomed-in image and schematic of the MATBG sample on the experiment resonator. The hBN/MATBG/hBN heterostructure is placed on an aluminum backgate to voltage-bias the MATBG and change its carrier density.

## Measuring the Kinetic Inductance and Critical Temperature of MATBG

The device is measured in a dilution refrigerator with a 20 mK base temperature ( $T_{\text{base}}$ ), and the effective temperature of the device with wiring connected is approximately 40 mK (see Method for details of the measurement setup and see Supplementary Information for the temperature characterization). Figure 2 shows the DC and microwave characterization of a representative MATBG device as a function of backgate voltage  $V_{\text{BG}}$ . The differential resistance  $dV/dI_{\text{DC}}$  is first measured with a standard 4-probe lock-in technique at zero bias current. As expected, the device is resistive at the charge neutrality point (CNP) at filling factor  $\nu = 0$ , and in the insulating regions at the filling factors  $\nu = \pm 2$  and  $\nu = +3$ . The resistance vanishes in the

vicinity of the insulating regions, near  $\nu \lesssim -2$  and  $\nu \gtrsim 2$ , indicating the onset of a superconducting phase for both hole-doped ( $\nu < 0$ ) and electron-doped ( $\nu > 0$ ) MATBG, respectively. We further parameterize the superconducting region by sweeping the DC bias current  $I_{\text{DC}}$  and backgate voltage  $V_{\text{BG}}$  in both the hole-doped (Fig. 2c) and the electron-doped (Fig. 2d) regimes.

We use a vector network analyzer (VNA) with ports 1 and 2 connected to the through-line to measure the microwave transmission coefficient  $S_{21}$  as a function of frequency, from which the resonance frequency of the resonator can be extracted.<sup>22</sup> Figure 2b plots the magnitude  $|S_{21}|$  as a function of frequency and back-gate voltage  $V_{\text{BG}}$ . There are two notable features in the data: 1) A constant resonant frequency  $f_r \approx 3.8$  GHz at the charge neutrality point  $\nu = 0$  and in the insulating regions at  $\nu = \pm 2$ , and 2) a backgate-dependent resonance frequency in the superconducting phase that begins just beyond the insulating regions,  $\nu \lesssim -2$  and  $\nu \gtrsim 2$ . Figures 2e and 2f show a close-up of the gate-dependent resonance lines in the hole-doped and the electron-doped regions, respectively. The resonance frequency is generally gate-dependent within the superconducting regions defined via the DC-transport measurements (Fig. 2c-d).

The presence and absence of resonator gate-dependence can be modelled with the lumped-element circuits<sup>23</sup> in Fig. 2g, representing the coplanar waveguide (CPW) terminated by MATBG under two different conditions. When the graphene is highly resistive, *i.e.*, at the CNP or in insulating states, the MATBG device is modeled as a resistor ( $R_{\text{TBG}} \gg 1$  k $\Omega$ ) in parallel with an inductive element  $L_{\text{prx}}$  (Fig. 2g, left schematic). The inductance  $L_{\text{prx}}$  represents the edge of the graphene that is in close proximity to the Ti/Al electrodes; the graphene edge “proximitizes” and becomes superconducting, inheriting its superconducting order parameter and robust doping from the superconducting Ti/Al. The inductance  $L_{\text{prx}}$  of the proximitized graphene is essentially constant, with no appreciable  $V_{\text{BG}}$ -dependence due to the robust doping, leading to a fixed, nominal resonance frequency (see Method and Refs.<sup>24,25</sup>). We determine  $L_{\text{prx}} = 1.32$  nH by taking a sufficiently large resistance for the insulating state,  $R_{\text{TBG}} = 100$  k $\Omega$ , and performing microwave simulations to reproduce the observed nominal resonance frequency  $f_0 = 3.8$  GHz.

In contrast, when the MATBG enters the superconducting phase, the resistance  $R_{\text{TBG}}$  vanishes and a kinetic inductance  $L_{\text{TBG}}$  arises from the superfluid condensate, resulting in a second parallel inductor that terminates the CPW and is  $V_{\text{BG}}$ -dependent (Fig. 2g, right schematic). Moreover, the resonance frequency  $f_r$  increases with the critical current, with both peaking at the same gate voltage. Outside the insulating and superconducting regions, the graphene bulk behaves like a normal metal with a small, non-zero resistance, which strongly damps the resonator and prevents an accurate extraction of the resonance frequency.<sup>22,23</sup>

Using this lumped-element model and the established value for  $L_{\text{prx}}$ , we perform microwave simulations to

extract the kinetic inductance of the MATBG device. We plot  $f_r$  as a function of  $1/L_{\text{TBG}}$  in Fig. 2h. The frequency shift  $\Delta f_r = f_r - f_0$  depends almost linearly on  $1/L_{\text{TBG}}$  (see Method for details).

We vary the refrigerator temperature to determine the MATBG critical temperature in the hole-doped and electron-doped regions (Figs. 3a and 3b). The critical temperature  $T_C^{(0.5)}$  – the temperature where the resistance is half of the normal-state resistance – is around 1 K across most of the gate-tunable area and consistent with previous reports on MATBG.<sup>3</sup> Other measures of critical temperature, including  $T_C^{(\text{onset})}$  as defined by the resistance kink, and  $T_C^{(\text{zero})}$  defined by zero resistance, are also plotted in Fig. 3 for comparison.  $T_C^{(\text{MW})}$  – the temperature where the resonance shift goes to zero – is comparable with  $T_C^{(\text{zero})}$  and  $T_C^{(0.5)}$ .

## Superfluid Stiffness and the Quantum Metric in MATBG

The “conventional” superfluid stiffness  $D_s^{(\text{conv})}$  from single-band Fermi liquid theory is inversely proportional to the charge carrier’s effective mass (Eq.2), which becomes exceedingly large for a nearly flat-band and even diverging in the flat-band limit, resulting in a diminishing  $D_s^{(\text{conv})}$  and no superconductivity. Yet, superconductivity is observed. It is proposed that this contradiction with experimental results could be resolved by considering the contribution from the non-trivial quantum geometry of the energy bands in these systems.<sup>1,13,14,16</sup> The quantum geometry here refers to the distance or curvature in the space formed by the electronic Bloch functions. It is characterized by the quantum geometric tensor (QGT), whose imaginary part is the well-known Berry curvature, and whose real part is called the quantum metric. The quantum metric quantifies the distance between two quantum states and establishes a lower-bound for the superfluid stiffness  $D_s$  in a flat-band superconductor.<sup>1</sup>

The kinetic inductance of MATBG enables us to directly measure the superfluid stiffness and its trends with physical parameters to test these ideas. Assuming the active MATBG region of our sample has the same aspect ratio as the actual device dimensions, length  $l$  and width  $w$ , the total measured superfluid stiffness  $D_s = (l/w)L_{\text{TBG}}$  at the base temperature  $T_{\text{base}}$  is plotted in Fig. 3c for hole-doping (blue) and electron-doping (orange). It exhibits a dome-shaped dependence on carrier density and is highly asymmetric with respect to the optimal doping, exhibiting steeper slopes in the under-doped regime and much greater values throughout the superconducting dome. For comparison, using the Fermi velocity  $v_F \simeq 10^3$  m/s near the  $\nu = \pm 2$  filling as reported in the literature<sup>19</sup> and assuming an isotropic (circular) Fermi surface with  $k_F = \sqrt{2\pi\tilde{n}}$ , the estimated conventional contribution  $D_s^{(\text{conv})} = e^2\tilde{n}v_F/\hbar k_F$  is plotted versus the effective carrier density  $\tilde{n}$  (measured with respect to  $|\nu|=2$ ) as a black dashed line in Fig. 3c.



The measured superfluid stiffness  $D_s$  is an order-of-magnitude larger than the conventional one,  $D_s^{(\text{conv})}$ . This discrepancy may be explained by considering the quantum geometry. At the magic angle, the superfluid stiffness  $D_s$  is predicted to be predominantly influenced by the quantum metric contribution  $D_s^{(\text{Q-m})}$ .<sup>13,14</sup> Our measurements indicate a maximum superfluid stiffness of  $1.7 \times 10^8 \text{ H}^{-1}$  for hole-doped MATBG and  $1.25 \times 10^8 \text{ H}^{-1}$  for electron-doped MATBG (Fig. 3c). Both are comparable with the theoretical prediction of  $0.7 \sim 4 \times 10^8 \text{ H}^{-1}$  of  $D_s^{(\text{Q-m})}$ .<sup>13,14</sup> This suggests that the dominant contribution to the superfluid stiffness in MATBG arises from quantum geometry.<sup>1,13–16,19,26,27</sup>

In 2D superconductors exhibiting the Berezinskii–Kosterlitz–Thouless (BKT) transition, the relationship between  $D_s$  and  $T_C$  is described by  $\frac{\pi \hbar^2 D_s(0)}{8e^2} \geq k_B T_C$ .<sup>28</sup> As illustrated in Fig. 3d by the black dashed line, the measured superfluid stiffness  $D_s(T_{\text{base}})$  – as determined by the kinetic inductance – and the critical temperature  $T_C$  determined by DC resistance measurements exhibit a relationship comparable with this formula, providing confidence in the accuracy of our experimental measurement of  $D_s$ .

These findings are all consistent with an interaction-driven, flat-band superconductor with a significant – even dominant – quantum geometric contribution to the underlying pairing mechanism.<sup>1,13–16,19,26,27</sup> We also observe that the measured  $D_s$  in this experiment aligns both qualitatively and quantitatively well with that extracted from measurements of critical-current density recently reported in.<sup>19</sup>

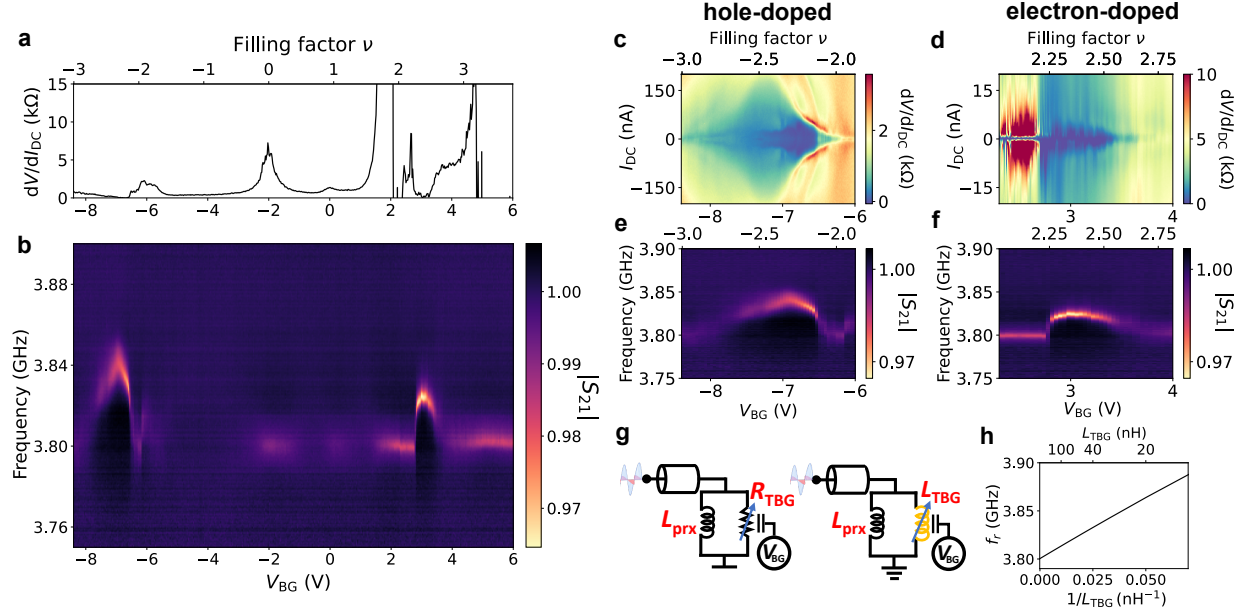


Figure 2: **Gate-voltage dependent DC and microwave characteristics.** **a** Differential resistance  $dV/dI_{DC}$  at zero bias current as a function of the backgate voltage  $V_{BG}$ . Top axis represents the filling factor  $\nu$ . **b** Microwave transmission coefficient  $|S_{21}|$  versus  $V_{BG}$ . The resonant frequency (bright line) shifts within the zero-resistance region in panel (a), near filling factors  $\nu = \pm 2$ . The resonance remains essentially constant within the high resistance region. **c,d**, Differential resistance  $dV/dI_{DC}$  as a function of  $V_{BG}$  and DC bias current  $I_{DC}$  within the superconducting region for hole-doped (**c**) and electron-doped (**d**) MATBG. Top axis represents the filling factor  $\nu$ . **e,f**, Zoomed-in view of the frequency shifts in panel (b) for the hole-doped superconducting region (**e**) and the electron-doped superconducting region (**f**). **g**, Lumped-element model for the resonator when voltage-biased in the highly-resistive regime (left panel) and the superconducting regime (right panel). See main text for a description of the circuit elements. **h**, Simulated resonance frequency  $f_r$  versus inverse of the MATBG kinetic inductance  $1/L_{TBG}$ . Top axis represents  $L_{TBG}$ .

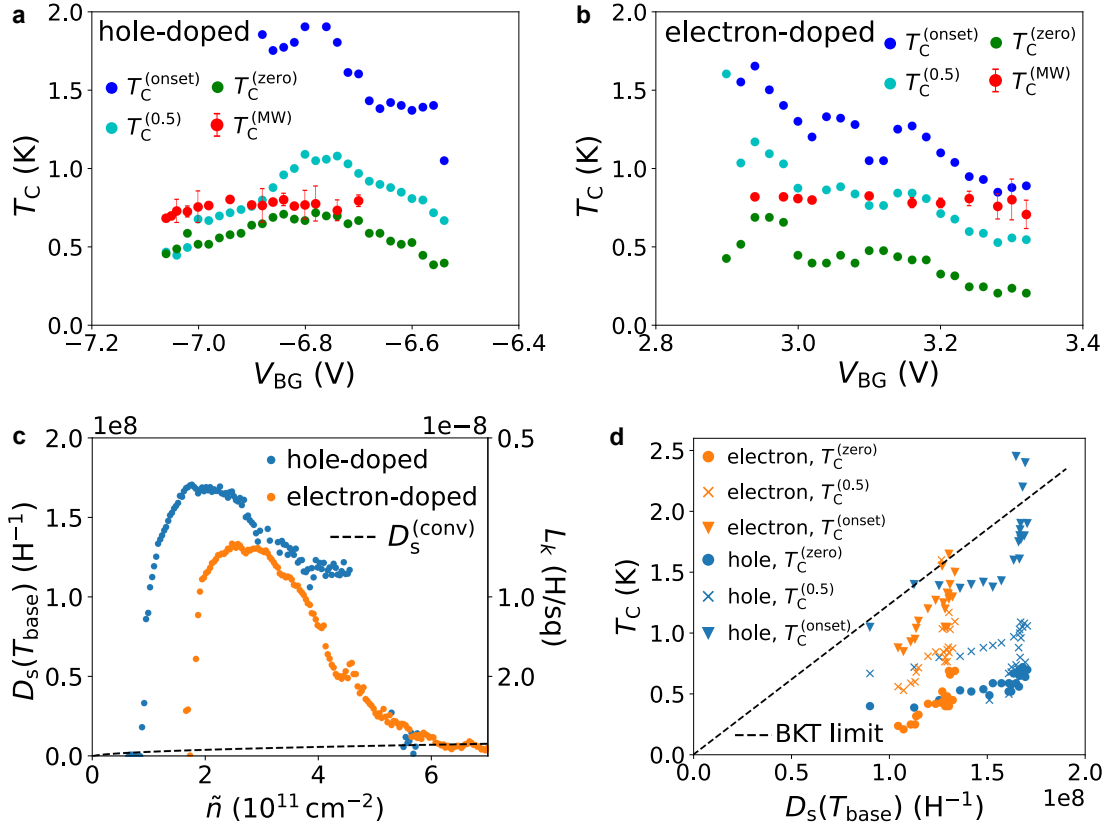


Figure 3: **Critical temperature and superfluid stiffness of superconducting MATBG.** **a,b** Backgate dependence of critical temperatures  $T_C^{(\text{onset})}$ ,  $T_C^{(0.5)}$ , and  $T_C^{(\text{zero})}$  as obtained from DC resistance measurements; and  $T_C^{(\text{MW})}$  as obtained from microwave measurements (see main text for definitions of critical temperatures) in the hole-doped (a) and the electron-doped (b) regimes. **c**, Superfluid stiffness  $D_s$  at base temperature  $T_{\text{base}}$  as a function of effective carrier density  $\tilde{n}$ , measured with respect to  $|\nu| = 2$ . The black dashed curve estimates the conventional contribution to the superfluid stiffness from single-band Fermi liquid theory:  $D_s^{(\text{conv})} = e^2 \tilde{n} v_F / \hbar k_F$ . **d**, Critical temperature  $T_C$  and corresponding superfluid stiffness  $D_s$  at base temperature  $T_{\text{base}}$  as tuned by  $V_{BG}$ . The black dashed line represents the BKT limit  $T_C = \pi \hbar^2 D_s(T_{\text{base}}) / 8e^2 k_B$ .

## Temperature Dependence of the MATBG Superfluid Stiffness

The temperature dependence of the superfluid stiffness and the associated quasiparticle spectrum has been widely used to probe the gap anisotropy in unconventional superconductors.<sup>29,30</sup> At low temperatures ( $T < 0.3 T_C$ ), the conventional superfluid stiffness  $D_s^{(\text{conv})}$  in superconductors with isotropic superconducting gaps exhibits an exponential temperature dependence  $\delta D_s^{(\text{conv})}(T) / D_s^{(\text{conv})}(0) \propto \sqrt{\frac{2\pi \Delta_0}{k_B T}} \exp(-\frac{\Delta_0}{k_B T})$ , where  $\delta D_s^{(\text{conv})}(T) = D_s^{(\text{conv})}(0) - D_s^{(\text{conv})}(T)$  is the change in stiffness with temperature  $T$ , and  $\Delta_0$  is the superconducting gap at zero temperature [20, 29]. In contrast, superconductors with an anisotropic gap or nodes exhibit a power-law temperature dependence  $\delta D_s^{(\text{conv})}(T) / D_s^{(\text{conv})}(0) \propto T^n$ .<sup>29</sup> In 2D momentum space, nodal gaps exhibit an exponent of  $n = 1$  in the clean limit, where the coherence length is shorter than the scattering

length of charge carriers. “Dirty” nodal gaps have  $n = 2$ , while nodeless anisotropic gaps display  $n > 2$ .<sup>31</sup> In this description, an exponential temperature dependence for isotropic s-wave gaps would correspond to  $n \rightarrow \infty$  for  $T \rightarrow 0$ .

On the other hand, recent theoretical studies of the quantum-metric contribution indicate that a power-law dependence on temperature is a general characteristic of  $D_s^{(Q-m)}$  in flat-band superconductors. Specifically, using a two-dimensional Lieb lattice model, an exponent of  $n = 5$  is predicted for an isotropic superconducting gap, while a smaller exponent around 3 is predicted for an anisotropic superconducting gap.<sup>32</sup>

To test these ideas, we study the flat-band superconductivity via the temperature dependence of the MATBG kinetic inductance. Figure 4 shows the temperature dependence of the resonant frequency in the superconducting phase for both the hole-doped and electron-doped regions. The change in frequency  $\Delta f_r = f_r(V_{BG}) - f_0$  is proportional to the superfluid stiffness (see Fig. 2h) and decreases with temperature. It eventually reaches zero at a temperature that matches the critical temperature as independently determined from DC resistance measurements. Note that the frequency shift attributed to the geometric inductance of the Al resonator and the proximitized graphene  $L_{prx}$  is considerably smaller than the  $V_{BG}$ -dependent frequency shift due to  $L_{TBG}$  (see Supplementary Information).

Figures 4a and 4b show  $\Delta f_r(T) / \Delta f_r(T_{base})$  – equivalent to  $D_s(T) / D_s(T_{base})$  – for temperatures  $T < T_{BKT}$ , where  $T_{BKT}$  is the Berezinskii–Kosterlitz–Thouless temperature (see Supplementary Information for the determination of  $T_{BKT}$ ) in the hole-doped ( $V_{BG} = -6.9$  V) and electron-doped ( $V_{BG} = 3.16$  V) regimes. The trends clearly deviate from the exponential dependence expected for a BCS isotropic model, indicating unconventional superconductivity in MATBG. Furthermore, they fit well to a power-law function with exponent  $n = 2.08$  and  $n = 2.44$ , respectively. The power-law dependence is also confirmed in the logarithmic plot of  $\Delta f_r(T_{base}) - \Delta f_r(T) \propto \delta D_s(T)$  depicted in Figures 4c and 4d. We extract the power-law exponent across the entire superconducting dome in both electron- and hole-doped regions, with  $n$  ranging from 2 to 3 (Fig. 4e and 4f). This is consistent with the expected behavior for an anisotropic superconducting gap using both the conventional model ( $D_s^{(conv)}$ ) and the quantum geometric model ( $D_s^{(Q-m)}$ ).<sup>29,30,32</sup> See the Supplementary Information for further analysis of anisotropy assuming  $D_s^{(conv)}$  and data from another sample showing similar results,  $n \sim 2$ .

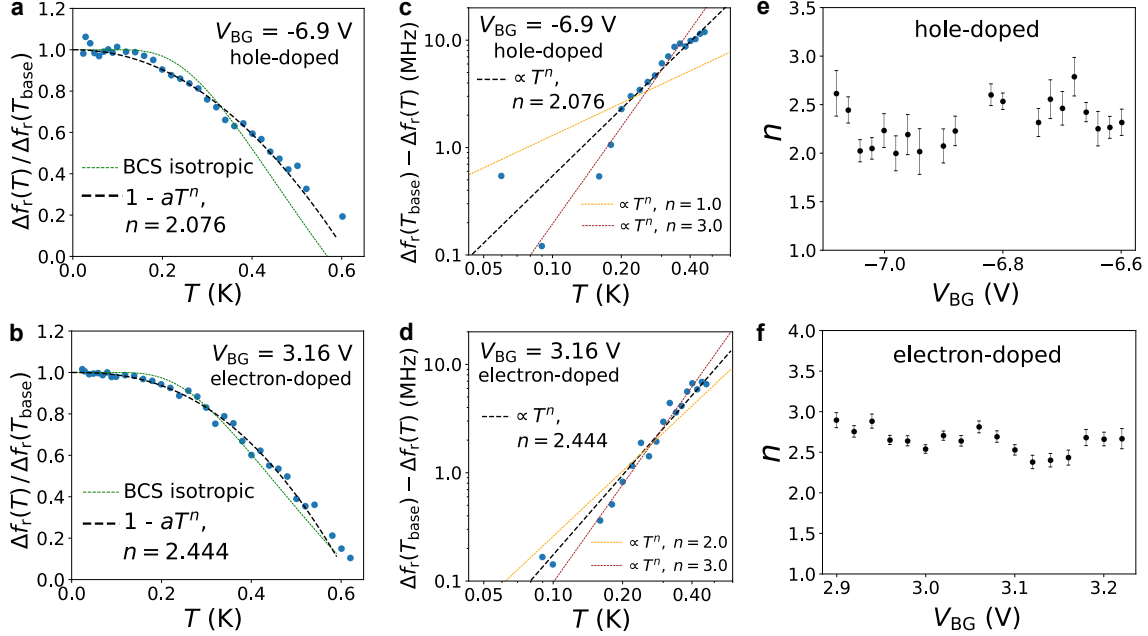


Figure 4: **Temperature-dependent shift in resonant frequency due to varying superfluid stiffness.** **a,b,** Temperature dependence of  $\Delta f_r(T)/\Delta f_r(T_{\text{base}})$  for  $T < T_{\text{BKT}}$  (See Supplementary Information for determination of  $T_{\text{BKT}}$ .) in the hole-doped (**a**) and the electron-doped (**b**) regimes. Blue dots represent the experimental data, black dashed lines depict the power-law fitting, and green dashed lines depict the exponential function in BCS isotropic model. **c,d,** Log-log plot of  $\Delta f_r(T_{\text{base}}) - \Delta f_r(T)$  in the hole-doped (**c**) and the electron-doped (**d**) regimes. Orange and brown dashed lines depict the power-law with exponent of  $n=1.0, 4.0$  and  $2.0, 4.0$ , respectively. **e,f,**  $V_{\text{BG}}$  dependence of the power-law fit exponent in the hole-doped (**e**) and the electron-doped (**f**) regimes.

## Bias Current and Microwave Power Dependence

We now explore the dependence of the superfluid stiffness on DC bias current. We apply a DC bias current through the DC terminal  $I_+$  (Fig. 1c). Figures 5a and 5b respectively display the DC differential resistance  $dV/dI_{\text{DC}}$  and the resonant frequency  $f_r$  versus DC bias current  $I_{\text{DC}}$  at  $V_{\text{BG}} = -6.7\text{ V}$ . Importantly,  $f_r$  shows a noticeable dependence for  $0 \leq I_{\text{DC}} \leq 40\text{ nA}$ , even around zero bias, whereas the DC resistance remains a constant  $0\ \Omega$ . The significant contrast between the microwave and DC measurements indicates a suppression of the superfluid stiffness within the superconducting state. At any given gate voltage, the frequency shift exhibits a quadratic dependence on the DC bias current (blue dashed line in Fig. 5b). A power-law fitting employed for all  $V_{\text{BG}}$  reveals that the quadratic dependence is manifest over the entire superconducting dome (Fig. 5c).

In addition, the resonant frequency  $f_r$  decreases linearly with the microwave power applied to the feedline (Fig. 5d). Considering that the microwave power is proportional to the square of the AC current amplitude,

$P \propto I_{\text{MW}}^2$ , this similarly indicates that the reduction of  $f_r$  depends quadratically on microwave current. Note that the power dependence of the MATBG-terminated resonator is driven primarily by the intrinsic MATBG response, as the contribution to the frequency shift from the Al resonator and the proximitized edges of the MATBG is negligibly small (see Supplementary Information).

The quadratic dependence on AC and DC currents can be understood as follows. Macroscopically, if spatial inversion symmetry is preserved in this system, a second-order nonlinearity is forbidden and the third-order inductive response becomes the leading order correction to the voltage, expressed as  $V = L_k(I) \frac{dI}{dt} = L_k^{(1)} \frac{dI}{dt} + L_k^{(3)} I^2 \frac{dI}{dt}$ . This explains a quadratic modulation of the superfluid stiffness on current amplitude. Microscopically, this behavior originates from the reduction of superfluid stiffness due to the finite phase gradient induced by currents less than the critical current and derived from Ginzburg-Landau equation, expressed as  $D_s(I)/D_s(0) = 1 - (I/I^*)^2$  or  $L_k(I) \propto L_0[1 + (I/I^*)^2]$ , where  $I^*$  is on the order of the critical current. These dependencies are commonly observed in many superconductors.<sup>33–38</sup>

In the context of nodal high- $T_C$  superconductors, theoretical discussions have proposed that the quadratic dependence of the conventional superfluid stiffness  $D_s^{(\text{conv})}$  on Meissner current may be replaced by a linear dependence above a current threshold set by the disorder,<sup>39–43</sup> known as the nonlinear Meissner effect. Our devices do not exhibit this effect as the quadratic dependence holds up to the  $I_C$  throughout the superconducting dome in all cases. It is important to note, however, that the nonlinear Meissner effect is not necessarily a universally observed characteristic of nodal superconductors<sup>44,45</sup> (see Supplementary Information). In addition, to our knowledge, the DC bias current dependence of quantum-metric superfluid stiffness  $D_s^{(\text{Q-m})}$  has not yet been discussed theoretically.

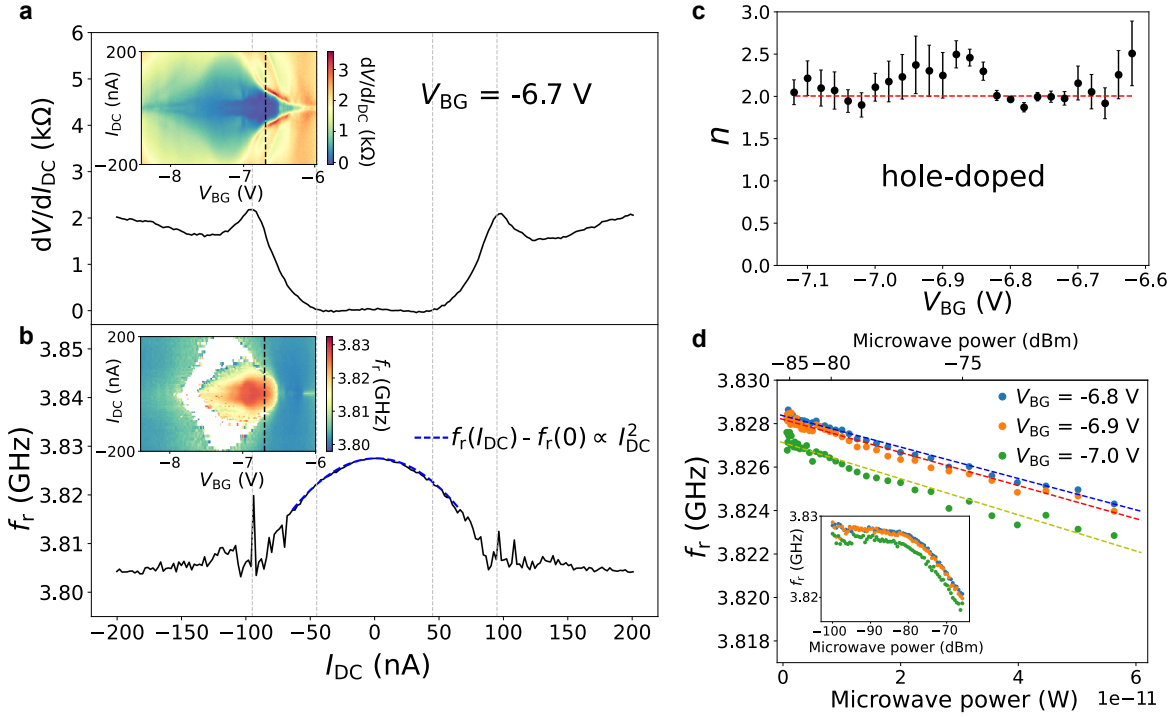


Figure 5: **DC Bias and microwave power dependence of resonant frequency.** **a**, Differential resistance  $dV/dI_{DC}$  dependence on bias current  $I_{DC}$  for backgate voltage  $V_{BG} = -6.7$  V (black dashed line in the inset). Inset: 2D color map versus  $V_{BG}$  and  $I_{DC}$ . **b**, Resonant frequency  $f_r$  dependence on  $I_{DC}$  for backgate voltage  $V_{BG} = -6.7$  V (black dashed line in the inset). Inset: 2D color map versus  $V_{BG}$  and  $I_{DC}$ . The blue dashed curve indicates a quadratic fit to the data. **c**, Exponents  $n$  of the power-law fitting  $f_r(I_{DC} = 0) - f_r(I_{DC}) \propto I_{DC}^n$  as a function of  $V_{BG}$ . Red dashed line indicates  $n = 2$ . **d**, Microwave power dependence of  $f_r$  at  $V_{BG} = -6.8, -6.9,$  and  $-7.0$  V. Blue dashed lines indicate a linear dependence with power, corresponding to a quadratic dependence on microwave current amplitude.

## Conclusion

Superconducting moiré systems hold great promise in both the fundamental sciences and emerging technologies. While many researchers, including the authors of this paper, have proposed and explored the application of these materials to quantum computing, here we leverage the microwave techniques that are commonly used to read out superconducting qubits to study these materials.

We use a superconducting microwave resonator terminated by a MATBG sample, configured to enable both DC and microwave measurements. With an internal quality factor of approximately 1000 and operation at a base temperature of 20 mK, this resonator-based platform can discern changes in the superconducting order parameter as small as one percent of the gap size. We use this platform to measure the MATBG kinetic inductance – a direct measurement of the superfluid stiffness – under various pair-breaking mechanisms, including thermal excitation, bias current, and microwave drive power.

In a flat-band system like MATBG, the superconducting phase cannot be fully described by the single-band Fermi liquid formalism, because the diverging effective mass of charge carriers leads to diminishing superfluid stiffness. Therefore, it has been proposed to explain flat-band superconductivity in a framework that incorporates quantum geometry as characterized by the topological quantum geometric tensor.<sup>1,15,16,27</sup> The quantum metric establishes a lower bound for superfluid stiffness in a flat-band superconductor. In MATBG, the quantum geometric effect is predicted to dominate the superfluid stiffness within a narrow range of the magic angle, substantially surpassing the conventional contribution derived from BCS and single-band Fermi liquid theory.<sup>1</sup>

We directly measure a MATBG superfluid stiffness that is an order-of-magnitude larger than predicted by single-band Fermi liquid theory. Rather, it aligns well with theoretical predictions incorporating quantum geometry that can explain flat-band superconductivity.<sup>1,13-16,26,27,32</sup> Our results are also consistent with recent experimental DC transport measurements,<sup>19</sup> underscoring the role of quantum geometry in superconducting MATBG.

The temperature dependence of the MATBG superfluid stiffness follows a power-law dependence with an exponent of 2 to 3 in both the hole-doped and electron-doped regions. This behavior clearly deviates from the exponential dependence observed in superconductors with isotropic s-wave pairing as well as the linear dependence observed in clean nodal superconductors. Within the framework of single-band Fermi liquid theory, a power-law exponent  $n = 2$  indicates a disordered nodal anisotropic gap and  $n > 2$  a nodeless anisotropic gap. Our data generally fall in the range  $n = 2 \dots 3$ , suggesting a highly anisotropic and possibly nodeless gap. We do observe  $n \approx 2$  for certain gate voltages, which may be consistent with a nodal gap in the presence of disorder, e.g., due to twist-angle variations.<sup>29,30</sup> If the quantum-geometry-dominated superfluid stiffness is instead considered, an exponent around 3 is also predicted for an anisotropic superconducting gap.<sup>32</sup> While it is beyond the scope of this experiment to distinguish the proportional contributions of single-band Fermi-liquid versus quantum-geometric superfluid stiffness, within both interpretations, our results indicate anisotropic pairing in MATBG and are consistent with quantum geometric effects.

The quadratic suppression of superfluid stiffness with DC bias and microwave current follows the Ginzburg-Landau theory and gives confidence that our kinetic-inductance measurement accurately portrays the superfluid stiffness. The quadratic dependence also aligns with a nodeless gap picture within the Fermi-liquid model. However, while it may also be consistent with a quantum geometric model, to our knowledge, this aspect of quantum geometry in superconductivity remains to be explored.

In summary, all of our measurements are consistent with a quantum geometric picture, where such theory



presently exists. In contrast, our results are only partially consistent with the single-band Fermi liquid picture, notably failing by over an order-of-magnitude in predicting the magnitude of the superfluid stiffness. Overall, our measurements suggest a clear connection between quantum geometry, superfluid stiffness, and anisotropic pairing in MATBG. Further theoretical study is needed to fully understand the impact of these experimental results.

## Methods

### Device fabrication

All devices are fabricated from a 250 nm-thick aluminum film deposited on high-resistivity Si chips. The resonators (Fig. 1a and 1b), are patterned with photo-lithography and wet etching of aluminum. Details of the aluminium fabrication process can be found in Ref.<sup>46</sup>

The incorporation of vdW heterostructures onto the patterned chips employs standard mechanical exfoliation and dry polymer-based techniques.<sup>21,25</sup> The hBN flake exfoliated on the SiO<sub>2</sub> substrate is transferred onto a Ti/Al (5/30 nm) back gate. After removing polymer by soaking in chloroform, the top surface of the hBN is cleaned by contact mode AFM scanning. Following an iterative stacking procedure, a stack of hBN and magic angle twisted bilayer graphene (MATBG) is released on the bottom hBN.

After transferring the heterostructures, the hBN/MATBG/hBN stack is shaped into Hall bar geometry using reactive ion etching (RIE). Then, superconducting contacts are made to the MATBG edge using RIE and thermal evaporation of Ti/Al. The superconducting bridging between the contacts and the aluminum resonator and the ground plane are made using an in-situ ion-mill followed by aluminum deposition.

### Measurement setup

The experiment is performed in a Bluefors XLD-1000 dilution refrigerator with a base temperature of  $\approx 20$  mK. Attenuation at several cryogenic stages is used to reduce excess thermal photons at higher-temperature stages from reaching the device. We use a -20 dB coupling to pump a Josephson travelling wave parametric amplifier (TWPA) mounted at base temperature to pre-amplify the resonator probe tone. To reduce reflection of the TWPA pump back to the device, we add a microwave isolator between the devices and the TWPA. Following the TWPA, there are additional isolators, filters, and a high-electron mobility transistor (HEMT) amplifier (LNF) thermally anchored to the 3K stage. At the room temperature (300K) stage, we further amplify (MITEQ) the output signal. Each DC line connected to the device is filtered at 3 K with a  $\pi$ -filter

and the QFilter (Quantum Machines) at the mixing chamber stage. See Extended Figure 1 for the schematics of the measurement setup.

## Microwave simulation

To determine the relationship between the resonant frequency shift and the kinetic inductance, we use the SONNET finite element solver. We model the device conductor as a two-dimensional perfect electrical conductor with a 350  $\mu\text{m}$  Silicon (Si) substrate and 500  $\mu\text{m}$  of vacuum above and below the model and calculate the S-parameters at the microwave ports.

We first test an intuitive model of our device that represents the MATBG kinetic inductance by an inductor (superconducting regime) or a larger resistor (insulating regime) in series with the effective inductance of the resonator;  $f_r = \frac{1}{2\pi\sqrt{(L_{\text{eff}}+L_{\text{TBG}})C_{\text{eff}}}}$ , where  $L_{\text{eff}}$  and  $C_{\text{eff}}$  are the effective geometric inductance and capacitance of the coplanar waveguide of the resonator, respectively. However, this model could not account for the continuous frequency shift from the insulating regime ( $\lambda/2$  resonator) to the superconducting regime ( $\lambda/4$  resonator).

Subsequently, we simulate a model with a parallel inductor – representing the always-superconducting proximitized edge of the graphene near the Ti/Al contacts – in parallel with the resistive or inductive impedance of the MATBG as discussed in the main text. We test the validity of this model with two additional experiments.

First, we fabricate a device, with the same geometry and metalization as the MATBG device, using a Bernal (AB)-stacked bilayer graphene. A resonance around 4 GHz in the highly insulating region (around the CNP) is observed (Extended Figure 2b). Since the Bernal-stacked bilayer graphene is non-superconducting, this observation indicates that the base resonance at around 4 GHz is not due to the intrinsic superconductivity of MATBG.

Second, we verify this model by applying a perpendicular magnetic field to the device. Extended Figure 2b shows the magnetic field dependence of the resonance in the bilayer graphene device gate-biased at the CNP. The resonance at 4.24 GHz vanishes at around 0.42 mT, which is much smaller than the critical magnetic field of either the resonator aluminum film ( $H_C \approx 10$  mT) or the superconducting MATBG, but consistent with a weak superconducting link to ground formed by proximitized graphene.<sup>47,48</sup> These tests verify the role of the proximitized graphene in maintaining a  $\lambda/4$  resonator with a resonance frequency that only shifts about 1% between insulating and superconducting MATBG regimes.

To analyze the lumped-element model, we set the resistance  $R_{\text{TBG}}=100$  k $\Omega$  to represent the insulating regime

and sweep  $L_{\text{prx}}$  to reproduce the observed base frequency of 3.8 GHz (Extended Figure 2d inset). This yields  $L_{\text{prx}}=1.32$  nH, consistent with a previous study on the Josephson inductance in proximitized graphene.<sup>49</sup> Using this value, we calculate the  $L_{\text{TBG}}$  dependence of the  $f_r$  (Extended Figure 2d). The frequency shift  $\Delta f_r = f_r - 3.8$  GHz depends almost linearly on  $1/L_{\text{TBG}} \propto D_s$ .

Throughout this simulation, the capacitance between the MATBG and the back gate is fixed at 3 fF, a value estimated based on the dimension and dielectric properties of the bottom hBN. We find that the resonance frequency is insensitive to this capacitance (Fig. Extended Figure 2c). Also, we check the  $L_{\text{TBG}}$  dependence of  $f_r$  with several different values of  $L_{\text{prx}}$ , as shown in Fig. Extended Figure 2d and e. The linear dependence between  $\Delta f_r$  and  $1/L_{\text{TBG}}$  holds for different values of  $L_{\text{prx}}$ , which justifies the analysis assuming  $\Delta f_r \propto D_s$ .

## References

1. Törmä, P., Peotta, S. & Bernevig, B. A. Superconductivity, superfluidity and quantum geometry in twisted multilayer systems. *Nat. Rev. Phys.* **4**, 528–542 (2022).
2. Cao, Y. *et al.* Correlated insulator behaviour at half-filling in magic-angle graphene superlattices. *Nature* **556**, 80–84 (2018).
3. Cao, Y. *et al.* Unconventional superconductivity in magic-angle graphene superlattices. *Nature* **556**, 43–50 (2018).
4. Cao, Y. *et al.* Strange metal in magic-angle graphene with near Planckian dissipation. *Phys. Rev. Lett.* **124**, 076801 (2020).
5. Andrei, E. Y. & MacDonald, A. H. Graphene bilayers with a twist. *Nat. Mater.* **19**, 1265–1275 (2020).
6. Park, J. M., Cao, Y., Watanabe, K., Taniguchi, T. & Jarillo-Herrero, P. Tunable strongly coupled superconductivity in magic-angle twisted trilayer graphene. *Nature* **590**, 249–255 (2021).
7. Hao, Z. *et al.* Electric field-tunable superconductivity in alternating-twist magic-angle trilayer graphene. *Science* **371**, 1133–1138 (2021).
8. Park, J. M. *et al.* Robust superconductivity in magic-angle multilayer graphene family. *Nat. Mater.* **21**, 877–883 (2022).
9. Zhang, Y. *et al.* Promotion of superconductivity in magic-angle graphene multilayers. *Science* **377**, 1538–1543 (2022).
10. Burg, G. W. *et al.* Emergence of correlations in alternating twist quadrilayer graphene. *Nat. Mater.* **21**, 884–889 (2022).

11. Oh, M. *et al.* Evidence for unconventional superconductivity in twisted bilayer graphene. *Nature* **600**, 240–245 (2021).
12. Cao, Y. *et al.* Nematicity and competing orders in superconducting magic-angle graphene. *Science* **372**, 264–271 (2021).
13. Hu, X., Hyart, T., Pikulin, D. I. & Rossi, E. Geometric and conventional contribution to the superfluid weight in twisted bilayer graphene. *Phys. Rev. Lett.* **123**, 237002 (2019).
14. Julku, A., Peltonen, T. J., Liang, L., Heikkilä, T. T. & Törmä, P. Superfluid weight and Berezinskii-Kosterlitz-Thouless transition temperature of twisted bilayer graphene. *Phys. Rev. B* **101**, 060505 (2020).
15. Xie, F., Song, Z., Lian, B. & Bernevig, B. A. Topology-bounded superfluid weight in twisted bilayer graphene. *Phys. Rev. Lett.* **124**, 167002 (2020).
16. Peotta, S. & Törmä, P. Superfluidity in topologically nontrivial flat bands. *Nat. Commun.* **6**, 8944 (2015).
17. Kim, H. *et al.* Evidence for unconventional superconductivity in twisted trilayer graphene. *Nature* **606**, 494–500 (2022).
18. Portolés, E. *et al.* Quasiparticle and superfluid dynamics in Magic-Angle Graphene. *Preprint at arXiv*. <https://arxiv.org/abs/2405.06793> (2024).
19. Tian, H. *et al.* Evidence for Dirac flat band superconductivity enabled by quantum geometry. *Nature* **614**, 440–444 (2023).
20. Tinkham, M. *Introduction to Superconductivity: Second Edition* (Dover Publications).
21. Wang, L. *et al.* One-dimensional electrical contact to a two-dimensional material. *Science* **342**, 614–617 (2013).
22. Probst, S., Song, F. B., Bushev, P. A., Ustinov, A. V. & Weides, M. Efficient and robust analysis of complex scattering data under noise in microwave resonators. *Rev. Sci. Instrum.* **86**, 024706 (2015).
23. Pozar, D. M. *Microwave engineering* (John Wiley & sons, 2011).
24. Schmidt, F. E., Jenkins, M. D., Watanabe, K., Taniguchi, T. & Steele, G. A. A ballistic graphene superconducting microwave circuit. *Nat. Commun.* **9** (2018).
25. Wang, J. I.-J. *et al.* Coherent control of a hybrid superconducting circuit made with graphene-based van der Waals heterostructures. *Nat. Nanotechnol.* **14**, 120–125 (2019).
26. Wu, F. Topological chiral superconductivity with spontaneous vortices and supercurrent in twisted bilayer graphene. *Phys. Rev. B* **99**, 195114 (2019).
27. Törmä, P. Essay: Where Can Quantum Geometry Lead Us? *Phys. Rev. Lett.* **131**, 240001 (2023).

28. Brun, C., Cren, T. & Roditchev, D. Review of 2D superconductivity: the ultimate case of epitaxial monolayers. *Supercond. Sci. Technol.* **30**, 013003 (2016).
29. Prozorov, R. & Giannetta, R. W. Magnetic penetration depth in unconventional superconductors. *Supercond. Sci. Technol.* **19**, R41 (2006).
30. Hardy, W., Kamal, S. & Bonn, D. *Magnetic penetration depths in cuprates: A short review of measurement techniques and results* (Springer US, 2002).
31. Hirschfeld, P. J. & Goldenfeld, N. Effect of strong scattering on the low-temperature penetration depth of a d-wave superconductor. *Phys. Rev. B* **48**, 4219 (1993).
32. Penttilä, R. P. S., Huhtinen, K.-E. & Törmä, P. Flat-band ratio and quantum metric in the superconductivity of modified Lieb lattices. *Preprint at arXiv*. <https://arxiv.org/abs/2404.12993> (2024).
33. Ku, J., Manucharyan, V. & Bezryadin, A. Superconducting nanowires as nonlinear inductive elements for qubits. *Phys. Rev. B* **82**, 134518 (2010).
34. Claassen, J., Adrian, S. & Soulen, R. Large non-linear kinetic inductance in superconductor/normal metal bilayer films. *IEEE Trans. Appl. Supercond.* **9**, 4189–4192 (1999).
35. Thomas, C. N., Withington, S., Sun, Z., Skyrme, T. & Goldie, D. J. Nonlinear effects in superconducting thin film microwave resonators. *New J. Phys.* **22**, 073028 (2020).
36. Vissers, M. R. *et al.* Frequency-tunable superconducting resonators via nonlinear kinetic inductance. *Appl. Phys. Lett.* **107** (2015).
37. Kirsh, N. *et al.* Linear and nonlinear properties of a compact high-kinetic-inductance WSi multimode resonator. *Phys. Rev. A* **16**, 044017 (2021).
38. Zhao, S., Withington, S., Goldie, D. J. & Thomas, C. N. Nonlinear properties of supercurrent-carrying single-and multi-layer thin-film superconductors. *J. Low Temp. Phys.* **199**, 34–44 (2020).
39. Dahm, T. & Scalapino, D. Nonlinear current response of a d-wave superfluid. *Phys. Rev. B* **60**, 13125 (1999).
40. Yip, S. & Sauls, J. Nonlinear Meissner effect in CuO superconductors. *Phys. Rev. Lett.* **69**, 2264 (1992).
41. Dahm, T. & Scalapino, D. Theory of microwave intermodulation in a high- $T_C$  superconducting microstrip resonator. *Appl. Phys. Lett.* **69**, 4248–4250 (1996).
42. Lee, S.-C. *et al.* Doping-dependent nonlinear Meissner effect and spontaneous currents in high- $T_C$  superconductors. *Phys. Rev. B* **71**, 014507 (2005).
43. Wilcox, J. *et al.* Observation of the non-linear Meissner effect. *Nat. Commun.* **13**, 1201 (2022).
44. Carrington, A., Giannetta, R., Kim, J. & Giapintzakis, J. Absence of nonlinear Meissner effect in  $\text{YBa}_2\text{Cu}_3\text{O}_{6.95}$ . *Phys. Rev. B* **59**, R14173 (1999).

45. Li, M.-R., Hirschfeld, P. & Wölfle, P. Is the nonlinear Meissner effect unobservable? *Phys. Rev. Lett.* **81**, 5640 (1998).
46. Yan, F. *et al.* The flux qubit revisited to enhance coherence and reproducibility. *Nat. Commun.* **7**, 1–9 (2016).
47. Bretheau, L. *et al.* Tunnelling spectroscopy of Andreev states in graphene. *Nat. Phys.* **13**, 756–760 (2017).
48. Ben Shalom, M. *et al.* Quantum oscillations of the critical current and high-field superconducting proximity in ballistic graphene. *Nat. Phys.* **12**, 318–322 (2016).
49. Schmidt, F. E., Jenkins, M. D., Watanabe, K., Taniguchi, T. & Steele, G. A. A ballistic graphene superconducting microwave circuit. *Nat. Commun.* **9**, 4069 (2018).
50. Raychaudhuri, P. & Dutta, S. Phase fluctuations in conventional superconductors. *Journal of Physics: Condensed Matter* **34**, 083001 (2021).
51. Jarjour, A. *et al.* Superfluid response of an atomically thin gate-tuned van der Waals superconductor. *Nat. Commun.* **14**, 2055 (2023).
52. Yong, J., Lemberger, T., Benfatto, L., Ilin, K. & Siegel, M. Robustness of the Berezinskii-Kosterlitz-Thouless transition in ultrathin NbN films near the superconductor-insulator transition. *Phys. Rev. B* **87**, 184505 (2013).
53. Makita, J., Sundahl, C., Ciovati, G., Eom, C. B. & Gurevich, A. Nonlinear Meissner effect in Nb<sub>3</sub>Sn coplanar resonators. *Phys. Rev. R* **4**. ISSN: 26431564 (1 2022).
54. Kannan, B. *et al.* On-demand directional microwave photon emission using waveguide quantum electrodynamics. *Nat. Phys.* **19**, 394–400 (2023).
55. Koch, J. *et al.* Charge-insensitive qubit design derived from the Cooper pair box. *Phys. Rev. A* **76**, 042319 (4 2007).
56. Hoi, I.-C. *et al.* Demonstration of a Single-Photon Router in the Microwave Regime. *Phys. Rev. Lett.* **107**, 073601 (7 2011).
57. Astafiev, O. *et al.* Resonance Fluorescence of a Single Artificial Atom. *Science* **327**, 840–843. ISSN: 0036-8075 (2010).
58. Hoi, I.-C. *et al.* Microwave quantum optics with an artificial atom in one-dimensional open space. *New Journal of Physics* **15**, 025011 (2013).
59. Mirhosseini, M. *et al.* Cavity quantum electrodynamics with atom-like mirrors. *Nature* **569**, 692–697 (2019).

## Acknowledgements

We acknowledge helpful discussions with Päivi Törmä, Leonid Levitov, Senthil Todadri, Masaki Roppongi, Kota Ishihara, Taisei Kitamura, and Yoichi Yanase. The authors thank Lamia Ateshian, David Rower, Patrick Harrington, and the device packaging team at MIT Lincoln Laboratory for technical assistance. This research was funded in part by the US Army Research Office grant no. W911NF-22-1-0023, by the National Science Foundation QII-TAQS grant no. OMA-1936263, by the Air Force Office of Scientific Research grant no. FA2386-21-1-4058, and by the Under Secretary of Defense for Research and Engineering under Air Force Contract No. FA8702-15-D-0001. P.J-H. acknowledges support by the National Science Foundation (DMR-1809802), the Gordon and Betty Moore Foundation’s EPiQS Initiative through Grant No. GBMF9463, the Fundacion Ramon Areces, and the CIFAR Quantum Materials program. D. R-L. acknowledges support from the Rafael del Pino Foundation. K.W. and T.T. acknowledge support from the JSPS KAKENHI (Grant Numbers 21H05233 and 23H02052) and World Premier International Research Center Initiative (WPI), MEXT, Japan. Any opinions, findings, conclusions or recommendations expressed in this material are those of the author(s) and do not necessarily reflect the views of the Under Secretary of Defense for Research and Engineering or the U.S. Government.

## Author Contributions

J.Î-j.W. conceived and designed the experiment. M.T., J.Î-j.W., T.H.D., and M.H. performed the microwave simulation. M.T., J.Î-j.W., T.H.D., S.Z., D. R-L., D.K.K., B.M.N., K.S., M.E.S. contributed to the device fabrication. M.T., J.Î-j.W., T.H.D., S.Z., D. R-L., A. A., and B.K. participated in the measurements. M.T., J.Î-j.W., and M.H. analyzed the data. K.W. and T.T. grew the hBN crystal. J.Î-j.W., M.T., and W.D.O. led the paper writing, and all other authors contributed to the text. J.A.G., T.P.O., S.G., P.J-H., J.Î-j.W., and W.D.O supervised the project.

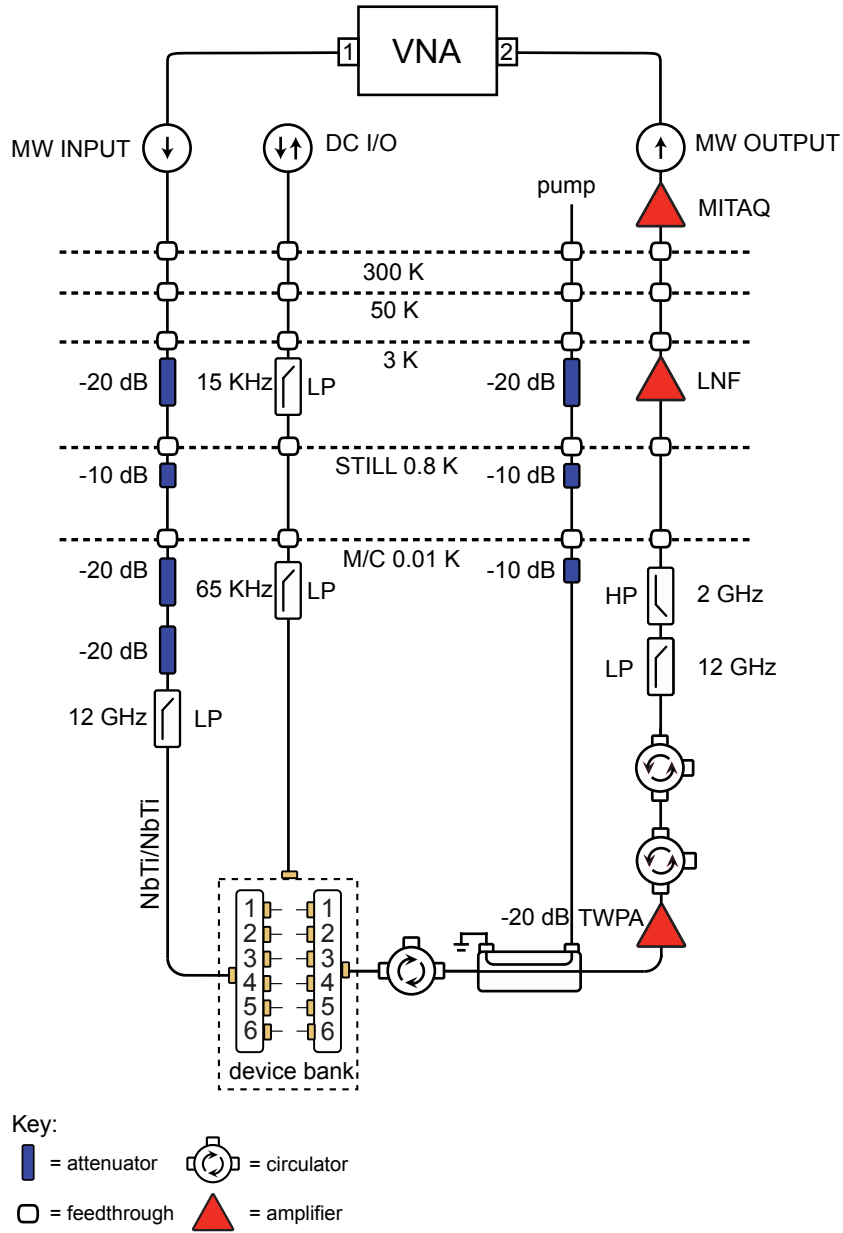
## Competing Interests Statement

The authors declare no competing interests.

## Correspondence and requests for materials

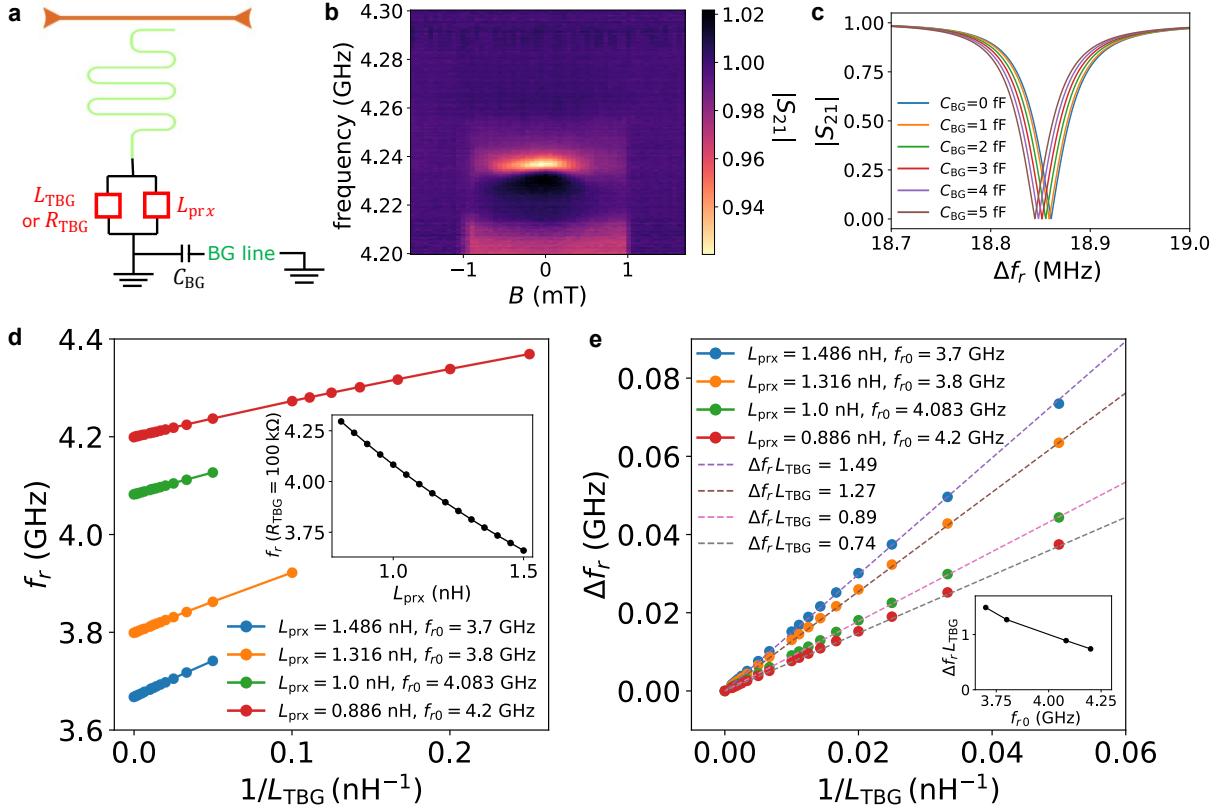
should be addressed to Joel Î-j. Wang, Pablo Jarillo-Herrero, or William D. Oliver.

# Extended data



Extended Figure 1: Wiring diagram of the microwave and DC characterization setup.





Extended Figure 2: **Simulation of resonance mode.** **a**, Model for the microwave simulation. **b**, Out-of-plane magnetic field dependence of the resonance of Bernal-stacked bilayer graphene near the charge neutrality point. **c**, Simulated  $|S_{21}|$  as a function of  $\Delta f_r = f_r - 3.8$  GHz for different values of  $C_{BG}$  of the model. **d**, Simulated resonance frequency as a function of  $1/L_{TBG}$  for different values of  $L_{prx}$ .  $C_{BG}$  is fixed at 3 fF. **e**, Data in **d**, where the offset resonance frequency at  $1/L_{TBG} = 0$  is subtracted. Dashed lines are the linear fit of the simulation data. Inset depicts the slope of the linear fit as a function of offset frequency  $f_{r0}$ , which depends on  $L_{prx}$ .

## Data availability

The data that support the findings of this study are available from the corresponding author upon reasonable request and with the cognizance of our US Government sponsors who funded the work.

## Supplementary Information

### 1 Aluminum control resonator and resonance in the insulating phase of MATBG

We characterize the aluminum control-resonator in the absence of MATBG to confirm that the MATBG-terminated resonator temperature and power dependence is dominated by the MATBG.

Fig. 8a plots the resonance frequency of the  $\lambda/4$  aluminum control resonator terminated directly to ground (i.e., without MATBG). Since the resonant frequency is  $f_r = \frac{1}{2\pi\sqrt{(L_G+L_k)C}}$ , where  $L_G (\gg L_k)$  is geometric inductance, the relation  $f_r(T_{\text{base}}) / f_r(T) - 1$  is proportional to  $L_k$ . The behavior is well fitted by the isotropic BCS model, which is consistent with the conventional superconductivity present in aluminum (see Fig. 8b). The shift in resonance frequency due to the kinetic inductance in the aluminum-only control resonator is much smaller than the MATBG-terminated aluminum experiment resonator, because the thickness of Al is much larger (250 nm) than that of MATBG ( $\sim 1\text{nm}$ ). This means the geometric inductance dominates in the aluminum-only resonator.

Fig. 8e presents the temperature dependence of the resonance for the MATBG-terminated resonator measured at the backgate voltage of  $V_{\text{BG}} = 2.44$  V in insulating region near  $\nu = 2$ . The temperature dependence remains flat below 0.5 K, in contrast to the resonance when biased in the superconducting phase, and is fitted by the isotropic BCS model with  $T_C$  of aluminum. We used this resonance frequency as a standard reference when analyzing the frequency shift due to the MATBG kinetic inductance.  $\Delta f_r$  in the main text is defined by  $\Delta f_r(V_{\text{BG}}, T) = f_r(V_{\text{BG}}, T) - f_r(V_{\text{BG}} = 2.44\text{V}, T)$ .

The microwave power dependence of  $f_r$  is negligible in both the aluminum-only resonator, and the MATBG-terminated resonator biased in the insulating region (Fig.8c and f). This indicates that the power dependence presented in the main text for the MATBG-terminated resonator is due to the MATBG superconductivity.

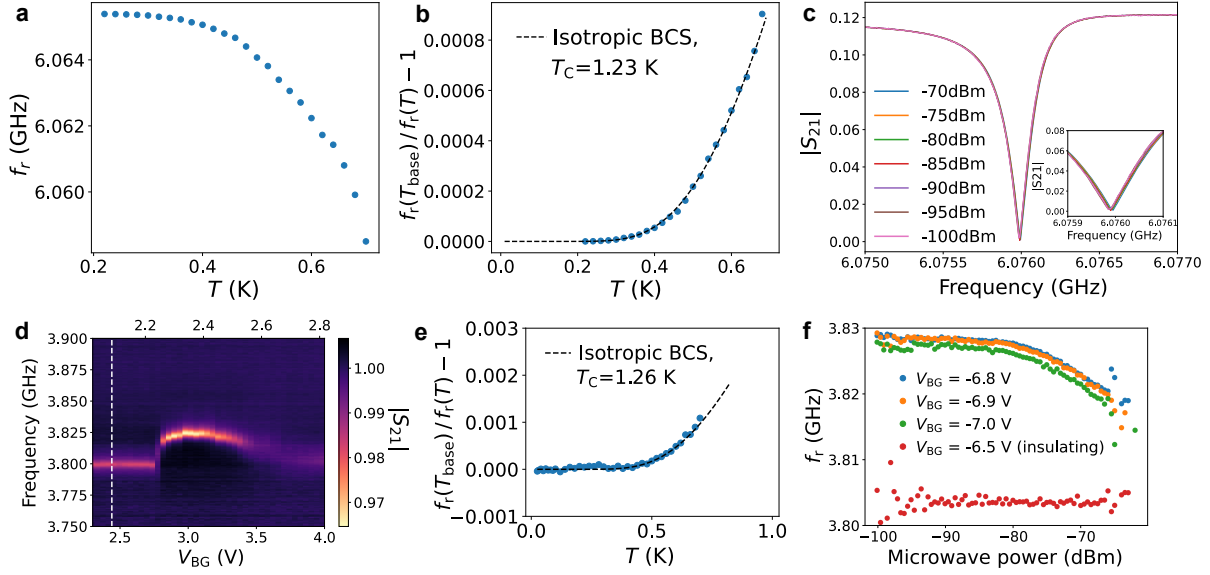


Figure 8: **Temperature and power dependence of the resonant frequency for the aluminum-only  $\lambda/4$  resonator (control resonator) and the MATBG-terminated resonator (experiment resonator) in the highly insulating region.** **a**, Temperature dependence of the resonance for the aluminum-only  $\lambda/4$  resonator. **b**, Temperature dependence of  $f_r(T_{\text{base}})/f_r(T) - 1$  for the aluminum-only  $\lambda/4$  resonator as fit with the isotropic BCS model. **c**,  $|S_{21}|$  for the aluminum-only  $\lambda/4$  resonator at  $T_{\text{base}}=20$  mK for different microwave powers. **d**, Gate dependence of the resonance in the MATBG-terminated resonator. The insulating region is indicated by a vertical white dashed line  $V_{\text{BG}}=2.44$  V. The frequency at this point is used as the reference point when determining a frequency shift. **e**, Temperature dependence of  $f_r(T_{\text{base}})/f_r(T) - 1$  for the MATBG-terminated resonator in the insulating region  $V_{\text{BG}}=2.44$  V. The resonance no longer shifts below about 0.5 K. **f**, Microwave power dependence of  $f_r$  at  $V_{\text{BG}}=-6.8, -6.9, -7.0$  V (where the MATBG is superconducting) and  $V_{\text{BG}}=-6.5$  V (where the MATBG is insulating).

## 2 Lorentzian fitting of the resonance

Fig. 9 shows an example of the Lorentzian fitting procedure of a resonance of MATBG resonator. The fitting function expression is:

$$S_{21}(f) = ae^{-\alpha - 2\pi ifd} \left[ 1 - \frac{(Q_l/Q_c)e^{i\phi}}{1 + 2iQ_l(f - f_r)/f_r} \right], \quad (3)$$

where  $a$  is a scaling coefficient determined by loss, attenuation, and amplification of the measurement line,  $\alpha$  is phase offset of the signal,  $d$  is length of the measurement line,  $Q_l = (Q_i^{-1} + Q_c^{-1})^{-1}$  is the loaded quality factor, with  $Q_i$  and  $Q_c$  being the internal- and coupling-quality factors, and  $f_r$  is the resonant frequency. By fitting  $S_{21}$  in the complex plane, we extract the following parameters:  $Q_i = 1044.7 \pm 28.5$ ,  $Q_c = 4161 \pm 54.4$ ,  $f_r = 4.2008154 \pm 0.0000737$  GHz.

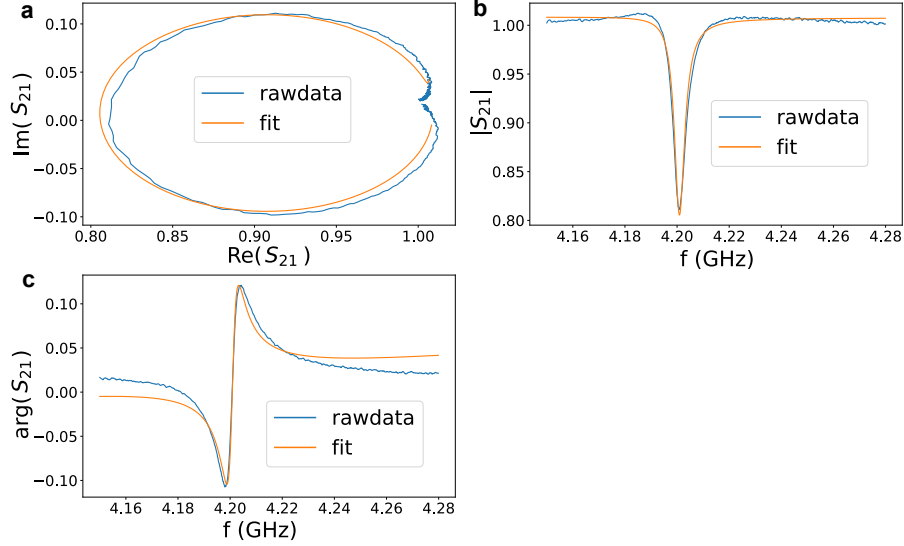


Figure 9: **Lorentzian fitting of the resonance.** **a**, Raw data of  $S_{21}$  (blue) and Lorentzian fitting (orange) plotted in the complex plane. **b**, Raw data and the Lorentzian fit of the magnitude of  $S_{21}$ . **c**, Raw data and the Lorentzian fit of the phase of  $S_{21}$ .

### 3 Fitting the temperature dependence with an extended s-wave model for conventional superfluid stiffness

The temperature dependence of the superfluid stiffness within single-band Fermi liquid theory  $D_s^{(\text{conv})}(T)$  is formulated using the Mattis-Bardeen equation as:<sup>20,29,30</sup>

$$\frac{D_s^{(\text{conv})}(T)}{D_s^{(\text{conv})}(0)} = 1 + \frac{1}{\pi} \int_0^{2\pi} d\phi \int_{\Delta(T,\phi)}^{\infty} \frac{\partial f}{\partial E} \frac{E}{\sqrt{E^2 - \Delta(T,\phi)^2}} dE, \quad (4)$$

where  $f$  is Fermi distribution function.

To model a superconducting gap with a continuous degree of anisotropy, we assume the following angle-dependent superconducting gap:

$$\Delta(T, \phi) = \Delta_0(T)g(\phi) = \Delta_0(T) \frac{1 + \alpha \cos(2\phi)}{\sqrt{1 + \alpha^2/2}}, \quad (5)$$

where  $\alpha = 0$  corresponds to an isotropic gap, and  $\alpha = 1$  is a nodal gap. The prefactor 2 in  $\cos(2\phi)$  is chosen without loss of generality of the rotational symmetry because the resulting temperature dependence  $D_s^{(\text{conv})}(T)$  does not depend on the prefactor.

Within a weak-coupling BCS theory,  $\Delta_0(T)$  is determined from the following self-consistent equation:

$$\int_0^\infty d\epsilon \int_0^{2\pi} d\phi \left[ \frac{\tanh\left(\frac{\epsilon^2 + \Delta_0^2(T)g^2(\phi)}{2T}\right)}{\sqrt{\epsilon^2 + \Delta_0^2(T)g^2(\phi)}} - \frac{\tanh\left(\frac{\epsilon}{2T_C}\right)}{\epsilon} \right] g^2(\phi) = 0. \quad (6)$$

Fig. 10a presents solutions of this equation for several anisotropy parameters  $\alpha$ . It is known that the solutions of the self-consistent gap equation can be approximated by the analytical formula:

$$\Delta_0(T) = \Delta_0(0) \tanh \left[ \frac{\pi T}{\Delta_0(0)} \sqrt{a(T_C/T - 1)} \right], \quad (7)$$

with two free parameters,  $a$  and  $\Delta_0(0)$  (Fig.10a). Substituting Eq.7 into Eq.5 and Eq.5 into Eq.4 yields  $\frac{D_s^{(\text{conv})}(T)}{D_s^{(\text{conv})}(0)}$  (solid lines in Fig.10b). In scanning tunneling microscope studies, Andreev reflection spectroscopy suggest a strong-coupling  $\Delta_0(0)/k_B T_C \simeq 3$  in MATBG.<sup>11</sup> Using this value and assuming  $a = 1$  in Eq.5, we obtain  $\frac{D_s^{(\text{conv})}(T)}{D_s^{(\text{conv})}(0)}$  (dashed lines in Fig. 10b).

Using this procedure for both the weak- and strong-coupling cases, we fit over a temperature range from the refrigerator base temperature to the Berezinskii-Kosterlitz-Thouless transition temperature  $T_{\text{BKT}}$ , determined by  $8e^2 k_B T_{\text{BKT}} / \pi \hbar^2 = D_s(T_{\text{BKT}})$  (see section 4), up to which this formulation is valid.<sup>50-52</sup> The results at  $V_{\text{BG}} = -6.9$  V and  $V_{\text{BG}} = 3.16$  V are shown with red and purple dashed lines in Figs. 11a and 11b, respectively, yielding anisotropy parameters  $\alpha = 0.52$  (weak), 0.76 (strong); and 0.44 (weak), 0.71 (strong). By performing the same fitting procedure over the superconducting dome, we obtain  $\alpha = 0.4 \sim 0.8$  for both the hole-doped and electron-doped regions (Figs. 11c-d). Critical temperatures obtained from this fitting are comparable with  $T_C$  determined from DC resistance measurements.

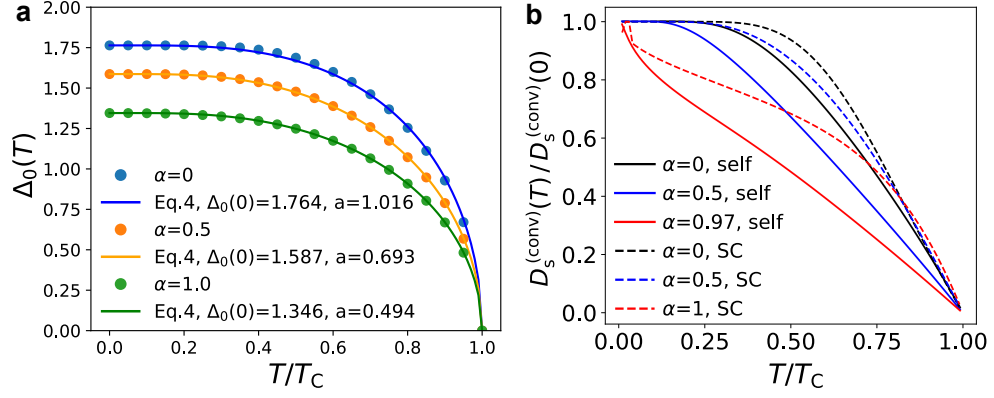


Figure 10: **Calculation of the temperature dependence of  $D_s^{(\text{conv})}$  based on the Mattis-Burdeen formula.** **a**, Self-consistently calculated  $\Delta_0(T)$  for different anisotropy parameters  $\alpha$ . Dots are the numerical results from the self-consistent equation, and lines are a fit using Eq. 7. **b**, Temperature dependence of  $n_s$  for different parameters of the formula. Black, blue, and red indicate anisotropy parameter  $\alpha = 0, 0.5, 1$ , respectively. For the solid lines (self),  $\Delta_0(0)$  and  $a$  in Eq. 7 are determined self-consistently using Eq. 6. For the dashed lines (SC, strong coupling), they are fixed at  $\Delta_0(0) = 3k_B T_C$  and  $a = 1$ .

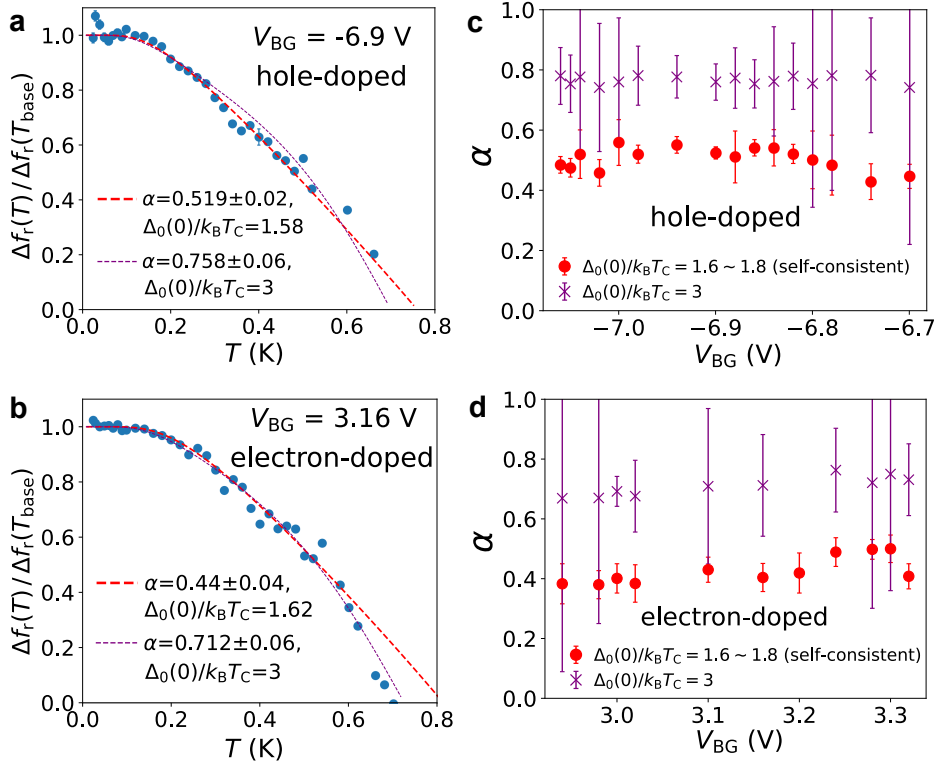


Figure 11: **Analysis of the temperature dependence based on the Mattis-Burdeen formula.** **a,b,** The temperature dependence of  $\Delta f_r(T) / \Delta f_r(T_{\text{base}})$  and fit functions based on the Mattis-Bardeen formula in the hole-doped (**a**) and the electron-doped (**b**) regimes. The red dashed curves represent best fits to an extended s-wave model using anisotropy parameters  $\alpha$  and  $T_C$  as fitting parameters, where  $\Delta_0(0)/k_B T_C$  is determined self-consistently. The purple dashed curves represent fittings with the fixed value of  $\Delta_0(0)/k_B T_C = 3$ . **c,d,** Backgate dependence of the anisotropy parameter  $\alpha$  obtained from fitting. Red and purple data points fit with the self-consistently determined  $\Delta_0(0)/k_B T_C$  and the  $\Delta_0(0)/k_B T_C = 3$ , respectively.

## 4 Berezinskii-Kosterlitz-Thouless transition and universal jumps

The Berezinskii-Kosterlitz-Thouless (BKT) theory of thermally excited vortex-antivortex pairs in 2D superconductors predicts a super-to-normal phase transition marked by a discontinuous drop in superfluid stiffness at a temperature  $T_{\text{BKT}}$  determined by the formula  $8e^2 k_B T_{\text{BKT}} / \pi \hbar^2 = D_s(T_{\text{BKT}})$ . The temperature dependence of the conventional superfluid stiffness below  $T_{\text{BKT}}$  follows the Mattis-Bardeen formula within the framework of Fermi liquid theory, and it exhibits an abrupt reduction at  $T_{\text{BKT}}$ , which is called a “universal jump”.<sup>50–52</sup> Therefore, power-law fitting in the main text and Mattis-Bardeen fitting in the previous section are done over the temperature range  $T < T_{\text{BKT}}$ .

Fig. 12 depicts the temperature dependence of the measured  $D_s$  and  $8e^2 k_B T / \pi \hbar^2$ , where  $T_{\text{BKT}}$  is determined by their intersection. It is difficult to discuss the universal jump due to the limited data and higher uncertainty

of the superfluid stiffness due to lower Q factor near  $T_C$ .

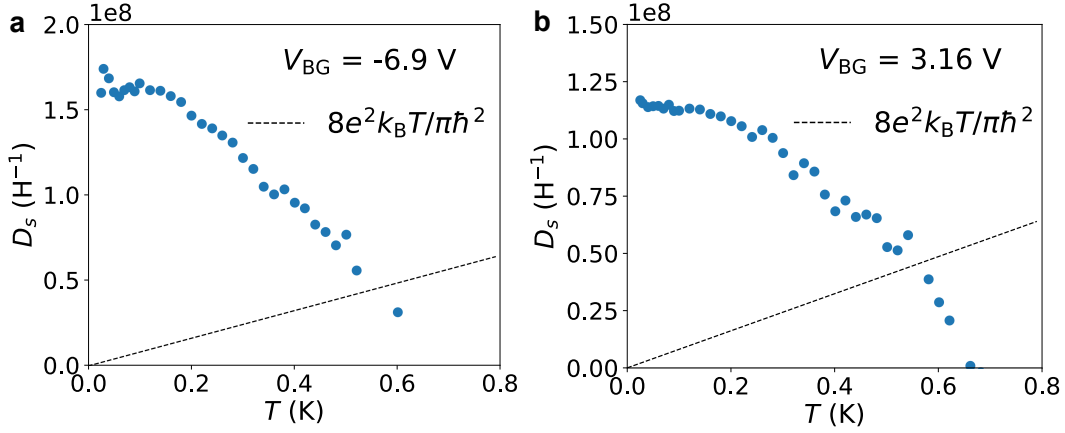


Figure 12: **Temperature dependence of the superfluid stiffness and determination of the BKT temperature.** **a,b**, Temperature dependence of  $D_s$  in hole-doped (a) and electron-doped (b) regimes, respectively. The intersection of the black dashed line and the data determine  $T_{\text{BKT}}$ .

## 5 Bias dependence in the electron doped regime

We observe a quadratic bias dependence in the hole-doped regime, where the critical current is well defined. In the electron-doped regime, the critical current is much smaller, likely due to smaller a spatial extent of the superconducting state (a larger effective aspect ratio leads to a larger effective current density in the superconducting region), see Fig. 13a. The bias dependence of the resonant frequency is linear instead of quadratic over the superconducting dome, as shown in Fig.13b. This bias dependence in the electron-doped regime likely indicates that the superconducting region comprises islands connected via narrow channels, where finite bias currents can readily break superconductivity in the narrow channels; consequently, the averaged superfluid stiffness rapidly decreases.

The nonlinear Meissner effect (NLME) has been discussed as an origin of the linear reduction in superfluid stiffness as a function of magnetic field or bias current in nodal superconductors.<sup>39–43</sup> Considering NLME under disorder effect, crossover from quadratic to linear dependence is theoretically expected, where the threshold current is proportional to the degree of disorder.<sup>39</sup> In our device, we observed linear dependence only in electron-doped region, which is affected more by disorder than hole-doped region inferred from the smaller critical current. This trend is opposite from the expected disorder dependence,<sup>39</sup> indicating the observed linear dependence in electron-doped region is not NLME. In addition, we have to note that the absence of the NLME has also been reported in the nodal superconductor YBCO [44, 45]. Also, the existence



of weak links can cause a linear dependence extrinsically in nodeless materials,<sup>53</sup> indicating that it is not a necessary condition nor a sufficient condition of nodal superconductivity.

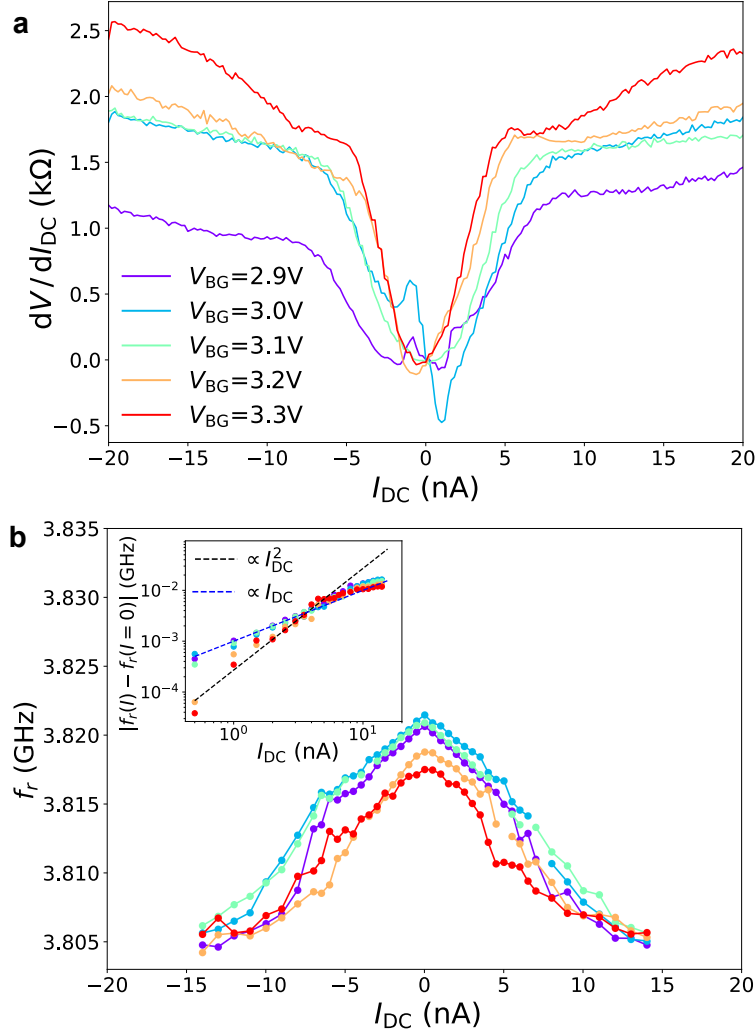


Figure 13: **Bias current dependence of the resistance and the resonant frequency in the electron-doped regime.** **a**, DC resistance  $R$  as a function of DC bias current  $I_{DC}$  for different  $V_{BG}$ . **b**, Resonant frequency  $f_r$  as a function of  $I_{DC}$ . Inset: Log-log plot of  $f_r(I) - f_r(0)$  versus  $I_{DC}$ . The blue and black dashed line indicate linear and quadratic dependence, respectively.

## 6 Additional sample

In another device with the same design and fabrication process, we observed qualitatively similar results, although it exhibited more spatial inhomogeneity, which results in multiple  $T_C$  and  $I_C$ . Fig. 14 shows the DC and microwave response of this second device as a function of  $V_{BG}$ . The behavior qualitatively matches the first device with the following notable differences: 1. the electron-doped superconducting

region does not exhibit complete zero-resistance whereas the first device shows zero resistance. 2. the hole-doped superconducting region shows multiple critical currents, which is thought to be due to the spatial inhomogeneity of the twist angle.

Fig. 15 presents the magnitude of the superfluid stiffness, which like the first device, is much larger than the conventional Fermi liquid theory would predict (Fig. 15c). The relation between  $T_C$  and  $D_s$  is consistent with the BKT theory (Fig. 15d).

Fig. 16 shows the temperature dependence in the hole-doped SC region. Although the temperature dependence of  $f_r$  and  $D_s$  have multiple steps due to having multiple regions with different  $T_C$  (Fig.16a and b), the low-temperature power-law analysis is still valid to extract the low energy excitation. Fig. 16c is the power-law exponent  $n$  obtained from the fitting at  $T < 0.3 T_C$ . The exponent is  $n = 1.3 \sim 3.2$ , which is comparable with the first device indicating an anisotropic pairing.

The DC bias dependence below the smallest  $I_C$  showed quadratic behavior and is also consistent with the first device (Fig.17).

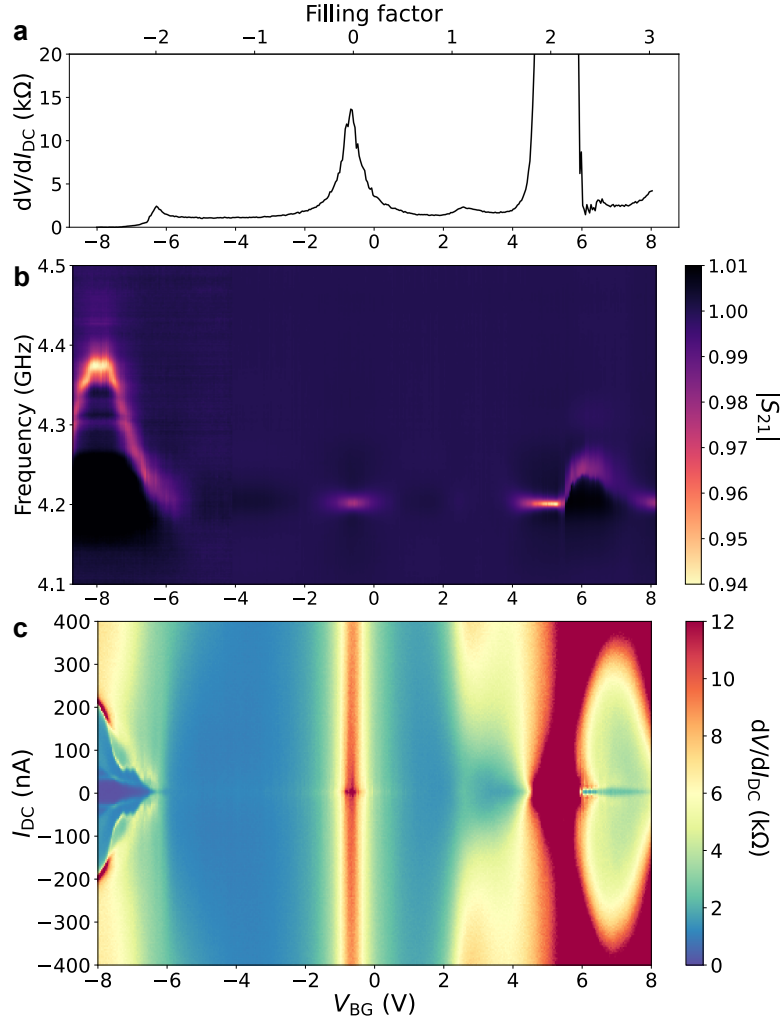


Figure 14: **Gate dependence of DC and microwave response in the second device.** **a**, DC resistance  $R$  as a function of the backgate voltage  $V_{BG}$ . Top axis represents the filling factor  $\nu$ . **b**, Microwave transmission coefficient  $|S_{21}|$  versus  $V_{BG}$ . The resonant frequency (bright line) shifts within the zero-resistance region in panel (a), near filling factors  $\nu = \pm 2$ . The resonance remains essentially constant within the high resistance region. **c**, Differential resistance  $dV/dI_{DC}$  as a function of  $V_{BG}$  and DC bias current  $I_{DC}$ .

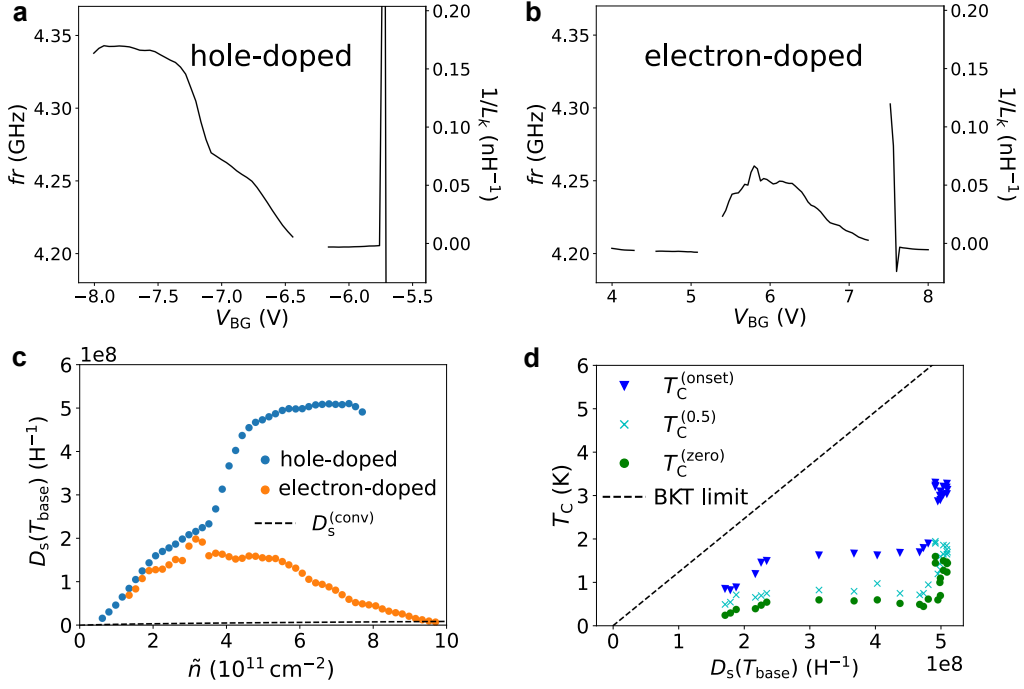


Figure 15: **Superfluid stiffness, carrier density, and critical temperature in the second device.** **a, b**, Frequency shift and inverse of the kinetic inductance as a function of  $V_{\text{BG}}$  in hole-doped (a) and electron-doped (b) regimes. **c**, Superfluid stiffness  $D_s$  at base temperature  $T_{\text{base}}$  as a function of effective carrier density  $\tilde{n}$ , measured with respect to  $|\nu| = 2$ . The black dashed curve estimates the conventional contribution to the superfluid stiffness from single-band Fermi liquid theory:  $D_s^{(\text{conv})} = e^2 \tilde{n} v_F / \hbar k_F$ . **d**, Critical temperature  $T_C$  and corresponding superfluid stiffness  $D_s$  at base temperature  $T_{\text{base}}$  as tuned by  $V_{\text{BG}}$ . The black dashed line represents the BKT limit  $T_C = \pi \hbar^2 D_s(T_{\text{base}}) / 8e^2 k_B$ .

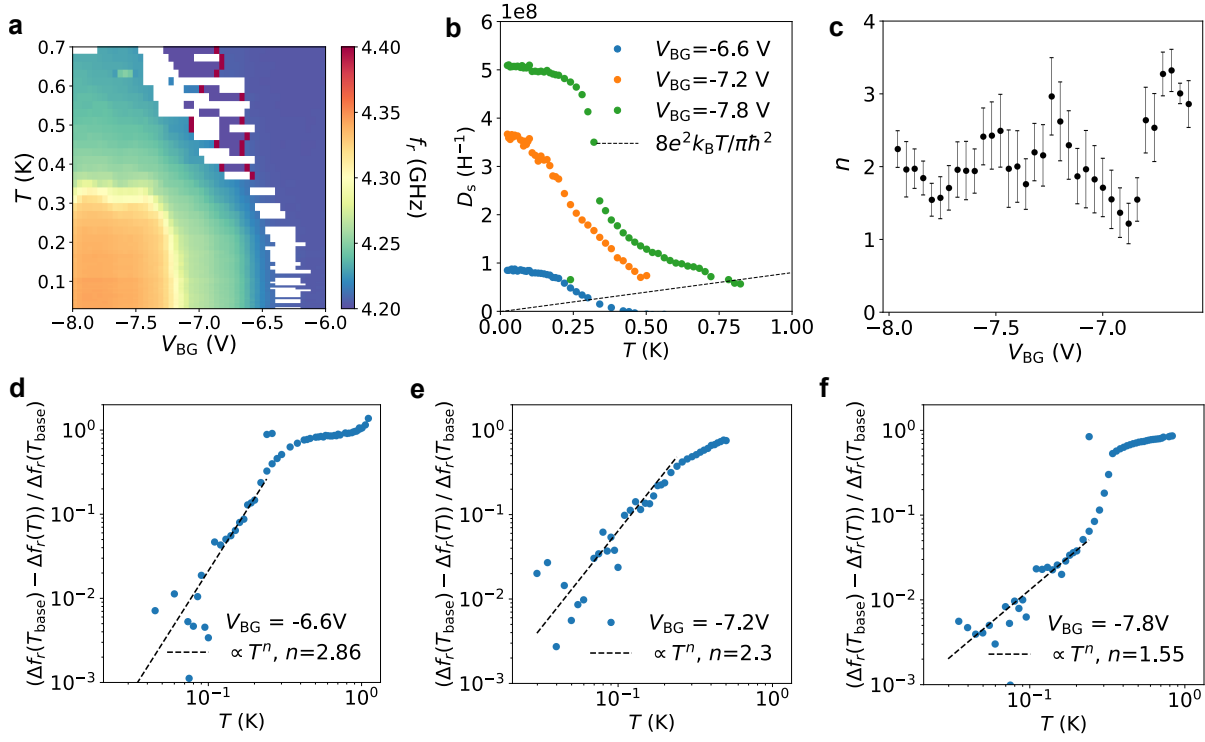


Figure 16: **Temperature dependence in the second device.** **a**, Resonance frequency  $f_r$  as a function of temperature and  $V_{BG}$ . **b**, Temperature dependence of the measured  $D_s$  at  $V_{BG}=-6.6$ ,  $-7.2$ , and  $-7.8$  V and  $8e^2 k_B T / \pi \hbar^2$  (black dashed line), where  $T_{BKT}$  is determined by their intersection. **c**,  $V_{BG}$  dependence of the exponent determined from the power-law fitting at  $T < 0.3 T_C$ . **d**, **e**, **f** Power-law fitting of  $(\Delta f_r(T_{base}) - \Delta f_r(T)) / \Delta f_r(T_{base})$  at  $V_{BG}=-6.6$ ,  $-7.2$ , and  $-7.8$  V.

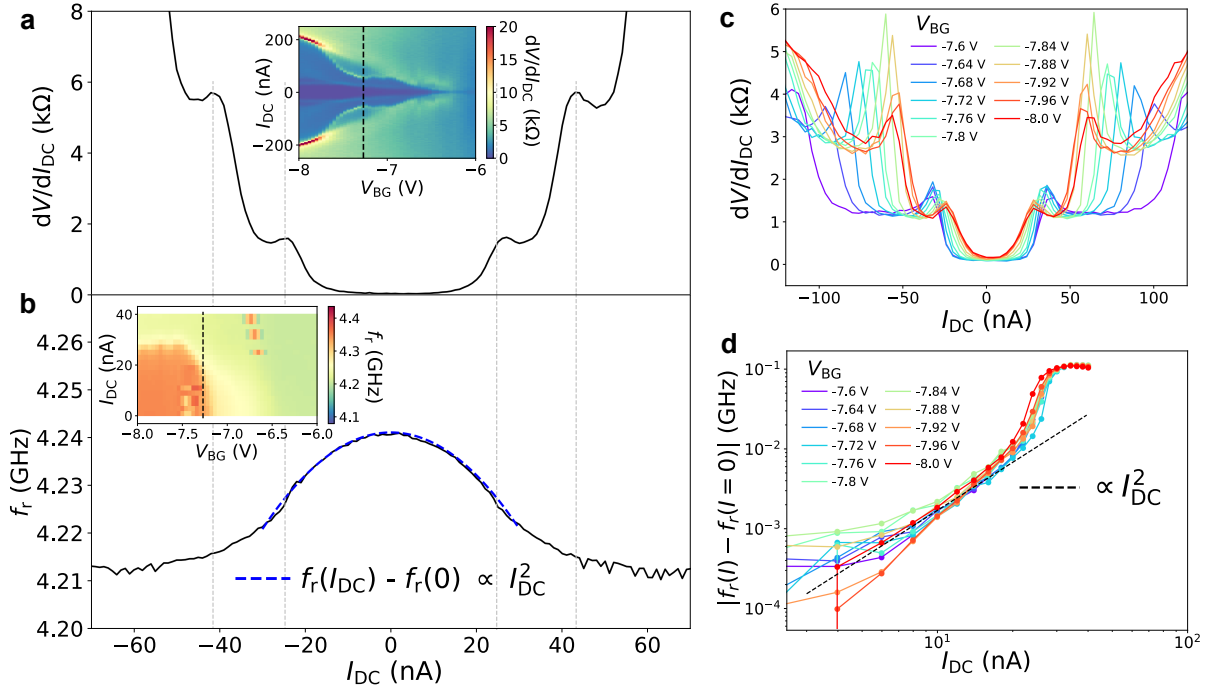


Figure 17: **DC bias current dependence in the second device.** **a**,  $I_{DC}$  dependence of the DC resistance  $dV/dI_{DC}$  at  $V_{BG} = -7.3$  V. Inset depicts the DC resistance as a function of  $I_{DC}$  and  $V_{BG}$ . **b**,  $I_{DC}$  dependence of  $f_r$  at  $V_{BG} = -7.3$  V. The blue dashed curve is the quadratic fit. Inset depicts  $f_r$  as a function of  $I_{DC}$  and  $V_{BG}$ . **c**,  $I_{DC}$  dependence of the DC resistance over the hole-doped SC region. **d**,  $I_{DC}$  dependence of  $|f_r(I) - f_r(I=0)|$  over the hole-doped SC region using a logarithmic scale. The black dashed line indicates the quadratic dependence.

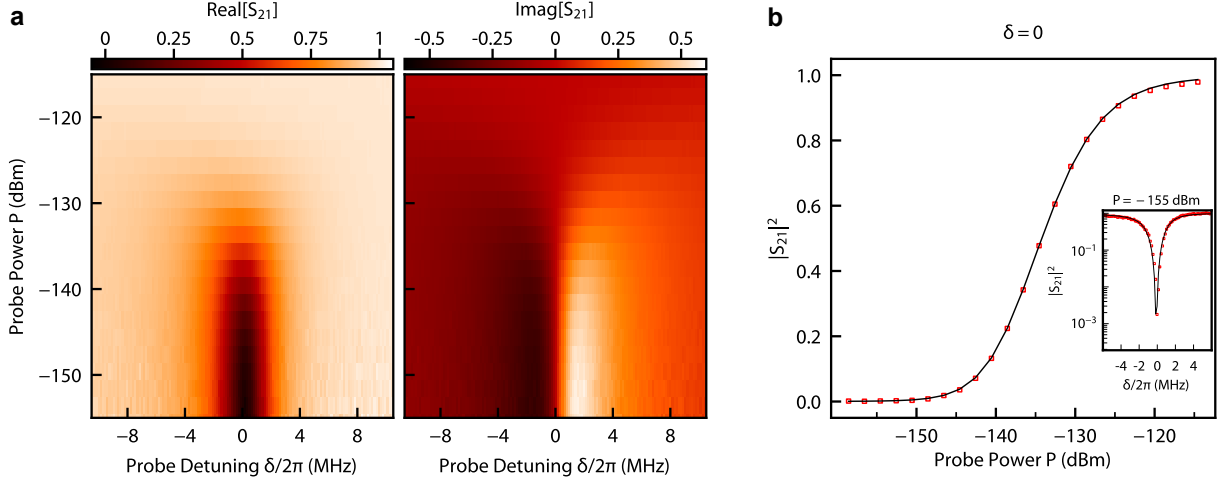


Figure 18: **Device temperature measurements with superconducting qubit spectroscopy.** **a** Real (left) and imaginary (right) components of the transmission spectrum of a coherent probe incident on a transmon qubit coupled to a coplanar waveguide as a function of the qubit-probe detuning  $\delta/2\pi$  and the probe power  $P$ . We extract the qubit-waveguide coupling rate  $\gamma/2\pi = 3.2$  MHz and the device temperature  $T = 41.21 \pm 1.39$  mK. **b** Transmittance  $|S_{21}|^2$  as a function of probe power  $P$  at zero qubit-probe detuning ( $\delta/2\pi = 0$ ). The measured data are plotted in red, and the theoretical fit is plotted in black. The inset shows the extinction in transmission in the form of a Lorentzian for a resonant probe at power  $P = -155$  dBm. The qubit acts as a single-photon mirror to resonant photons that arrive at the qubit on-average in the single-photon limit and smaller.

## 7 Device Effective Temperature Measurement

We measure the effective temperature of superconducting qubits that share the same mixing chamber of the dilution refrigerator and similar driving lines.<sup>54</sup> We strongly couple a transmon qubit<sup>55</sup> at frequency  $\omega/2\pi = 4.88$  GHz to an open coplanar waveguide with coupling strength  $\gamma/2\pi = 3.2$  MHz. We send a coherent probe into the waveguide and measure the elastic scattering of the qubit.<sup>54</sup>

In the single-photon limit and less, the qubit absorbs and re-emits the photon in the forward and backward directions with a phase shift. The results ideally perfect destructive interference in the forward direction and perfect constructive interference in the backward directly. This results in the extinction of the transmission signal for probes with low average photon numbers  $|\alpha|^2 \ll 1$ .<sup>56–58</sup> The master equation for the simplified model of a single qubit coupled to a waveguide is given by [59],

$$\partial_t \hat{\rho} = \frac{1}{i\hbar} [\hat{H}, \hat{\rho}] + (\bar{n}_{\text{th}} + 1) \gamma D[\hat{\sigma}^-] \hat{\rho} + \bar{n}_{\text{th}} \gamma D[\hat{\sigma}^+] \hat{\rho} + \frac{\gamma_\phi}{2} D[\hat{\sigma}_z] \hat{\rho}. \quad (8)$$

The single-qubit Hamiltonian is  $\hat{H} = \frac{1}{2} \delta \hat{\sigma}_z + \frac{1}{2} \Omega_p \hat{\sigma}_x$ , where  $\gamma_\phi$  is the pure dephasing rate of the qubit,

$\delta = \omega - \omega_p$  is the qubit-probe detuning, the Lindblad dissipator is  $D[\hat{O}] = \hat{O}\hat{\rho}\hat{O}^\dagger - \frac{1}{2}\{\hat{O}^\dagger\hat{O}, \hat{\rho}\}$ , and  $\Omega_p = \sqrt{2\gamma P/\hbar\omega_p}$  is the drive strength of the probe with power  $P$ . The qubit is coupled to a thermal bath of photons present in the waveguide, with temperature  $T$  and average thermal photon number  $\bar{n}_{\text{th}} = 1/(e^{\frac{\hbar\omega_q}{k_B T}} - 1)$ .

Assuming that the probe propagates towards the right, the rightward propagating output of the waveguide can be determined via input-output theory:

$$\hat{a}_R = \hat{a}_R^{\text{in}} + \sqrt{\frac{\gamma}{2}}\hat{\sigma}^-. \quad (9)$$

Therefore, we can calculate  $S_{21} = \langle \hat{a}_R \rangle / \langle \hat{a}_R^{\text{in}} \rangle$ ,<sup>59</sup>

$$S_{21}(\delta, \Omega_p) = 1 - \frac{\gamma(1 + i\delta/\gamma_2^{\text{th}})}{2\gamma_2^{\text{th}}(2\bar{n}_{\text{th}} + 1)[1 + (\delta/\gamma_2^{\text{th}})^2 + \Omega_p^2/(\gamma_1^{\text{th}}\gamma_2^{\text{th}})]}. \quad (10)$$

We define a thermally enhanced decay and dephasing rate,  $\gamma_1^{\text{th}} = (2\bar{n}_{\text{th}} + 1)\gamma$  and  $\gamma_2^{\text{th}} = \gamma_1^{\text{th}}/2 + \gamma_\phi$ , where  $\gamma_2 = \gamma/2 + \gamma_\phi$  is the bare decoherence rate. Transmission measurements as a function of probe power  $P$  and detuning  $\delta$ , as shown in Fig. 18, enable us to extract the device effective temperature  $T = 41.21 \pm 1.39$  mK. These measurements also calibrate the absolute power of microwave tones incident on devices.